Cellular-Scale Imaging of Transparent Retinal Structures and Processes Using Adaptive Optics Optical Coherence Tomography

Donald T. Miller, **Kazuhiro Kurokawa**

School of Optometry, Indiana University, Bloomington, Indiana 47405, USA

Abstract

High-resolution retinal imaging is revolutionizing how scientists and clinicians study the retina on the cellular scale. Its exquisite sensitivity enables time-lapse optical biopsies that capture minute changes in the structure and physiological processes of cells in the living eye. This information is increasingly used to detect disease onset and monitor disease progression during early stages, raising the possibility of personalized eye care. Powerful high-resolution imaging tools have been in development for more than two decades; one that has garnered considerable interest in recent years is optical coherence tomography enhanced with adaptive optics. State-of-the-art adaptive optics optical coherence tomography (AO-OCT) makes it possible to visualize even highly transparent cells and measure some of their internal processes at all depths within the retina, permitting reconstruction of a 3D view of the living microscopic retina. In this review, we report current AO-OCT performance and its success in visualizing and quantifying these once-invisible cells in human eyes.

Keywords

adaptive optics; optical coherence tomography; ophthalmoscopy; retina; structure and function

1. INTRODUCTION

There has been remarkable progress in the development of high-resolution retinal imaging tools in the past two decades. Key technologies include adaptive optics (AO), scanning laser ophthalmoscopy (SLO), fundus ophthalmoscopy, and optical coherence tomography (OCT) (see the sidebar titled Description of Optical Coherence Tomography). Parallel to these developments have been major advances in processing retinal images. The literature already contains an abundance of recent excellent reviews on high-resolution retinal imaging, mostly on the combination of AO and SLO (AO-SLO), including two in this journal (Roorda &

Duncan 2015, Cole et al. 2016, Merino & Loza-Alvarez 2016, Morgan 2016, Burns et al. 2018, Georgiou et al. 2018, Paques et al. 2018, Gill et al. 2019, Hunter et al. 2019), and on the combination of AO and OCT (AO-OCT) (Jonnal et al. 2016, Dong et al. 2017, Pircher & Zawadzki 2017), the subject of this review. The existence of these reviews raises the question: Why another?

AO-OCT was first applied to the human eye in the early 2000s (Miller et al. 2003, Hermann et al. 2004, Zawadzki et al. 2005, Zhang et al. 2005), and its performance has steadily increased since then. While these developments have been captured in prior reviews, they are often framed by what AO-OCT can achieve after all of its technological problems are overcome—capturing pristine 3D views of the cellular retina that are not possible using other imaging modalities such as AO-SLO and AO fundus ophthalmoscopy. Over the past few years, however, there have been critical AO-OCT advancements in high-speed OCT image acquisition, real-time image reconstruction and display, and 3D image registration that finally thrust AO-OCT over its formidable technological barriers. Today, state-of-the-art AO-OCT is able to visualize highly transparent cells and cell components and measure cell processes manifested as micrometer- and nanometer-scale optical changes. This work has garnered considerable interest in both the scientific and clinical communities. With many new results, there is a need to review current AO-OCT performance in visualizing transparent retinal cells and cell processes in the living human eye, recent successes in seeing these once-invisible cells, and remaining challenges. It is in this context that we write this article. For conciseness, we concentrate entirely on the human retina.

2. IMAGING REQUIREMENTS

Visualization of single retinal cells and their processes through the intact optics of the human eye is largely governed by three main requirements, regardless of imaging modality. These are spatial resolution (smallest cellular detail to be resolved in the retina; Figure 1a), sensitivity (weakest signal to be detected in the retina, which we limit to tissue reflections, not fluorescence or indirect scatter; Figure 1b), and temporal bandwidth (from fastest to slowest cellular change to be detected in the retina).The requirements are determined by the properties of the retinal tissue to be imaged and by the optics of the eye (the cornea, lens, and iris) that perform as the objective lens and aperture of the imaging system. We discuss each requirement in this section; in Section 3, we discuss how AO-OCT achieves them.

2.1. Spatial Resolution (Smallest Cellular Detail to Be Resolved)

The retina is composed of tightly packed neurons whose major components (somas, axons, and dendrites) organize loosely into stacked layers, with somas of similar type often forming regular mosaics (Boycott et al. 1969, Hogan et al. 1971). This characteristic packing is readily apparent in the histologic cross-section in Figure 2. Visualizing an individual cell or cell component in the retina requires resolving it from its neighbors, both those laterally adjacent to it and those stacked above and below it. This dictates a 3D resolution no worse than the size of the cell or cell component to be imaged, e.g., 7–8 μm for bipolar cell somas, but even better resolution may be necessary to resolve the gaps between cells that define their boundaries. Better resolution is also necessary to delineate the smaller cell axons and

dendritic processes, whose maximum caliber is no larger than a couple of microns, and substantially higher resolution is needed for subcellular structures (organelles), which approach the nanometer scale. As depicted in Figure 1a, light microscopy permits observation of retinal cell components down to the size of organelles (ex vivo), while electron microscopy supports viewing of components down to the size of molecules (subnanometer to nanometer). In vivo imaging through the eye's optics by clinical ophthalmoscopes is strikingly worse owing to optical performance limitations of the ocular media and the finite size of the eye's pupil. Aberrations in the cornea and crystalline lens and diffraction caused by the eye's pupil limit spatial resolution at the retina to approximately 15 μm transversely and 300 μm axially, as shown in Figure 1a. These dimensions are noticeably larger than the size of most cells and cell components in the retina, preventing their resolution without more powerful imaging methods.

2.2. Sensitivity (Weakest Reflectance to Be Detected)

Most retinal cells are transparent to maximize light throughput to the photoreceptors lying underneath. This results in exceedingly little light being backscattered from these cells, making them difficult to detect (poor signal-to-noise ratio) and difficult to differentiate from adjacent cells (poor cell contrast). Other cells—e.g., retinal pigment epithelium (RPE) cells, blood cells, and cells that compose the vasculature—backscatter notably more because of their high concentrations of pigment granules with a greater refractive index than their surround, yielding higher signal-to-noise ratios.

As illustrated in Figure 1b, the entire fundus (retina, choroid, and sclera) scatters between 0.1% and 10% (−30 dB to −10 dB) of the light that enters the eye, depending on wavelength, back through the pupil (Delori & Pflibsen 1989). Red and near-infrared wavelengths are at the upper end of this range (10%), while short wavelengths in the blue spectrum are at the lower end (0.1%). A notable portion of this fraction, however, does not contribute meaningfully to the conventional fundus image because it contains light that has scattered multiple times in the tissue, creating a uniform veil of background light that reduces image contrast. When viewed directly, only light singly scattered from the point where the imaging beam is focused provides information about that location. Of course, fluorescence and multiply scattered light can also provide information when examined using specialized viewing methods based on intrinsic and extrinsic fluorophores and dark field microscopy (indirect viewing) (Chui et al. 2012, Scoles et al. 2014, Burns et al. 2018, Hunter et al. 2019, Jung et al. 2019, Laforest et al. 2020). While powerful, these methods do not detect single scatter, the focus of this review.

Flood-illuminated fundus ophthalmoscopes detect all of the backscattered light, whether singly or multiply scattered. Thus, an appreciable portion of the light that they capture carries little high-fidelity information, as depicted in their images. In contrast, clinical OCT is significantly more sensitive to singly than to multiply scattered light (Izatt et al. 2015). As shown in Figure 1b, singly scattered reflectances of the main retinal layers, obtained using clinical OCT, are much weaker than the clinical ophthalmoscope total reflectance. The strongest backscatter as measured with OCT occurs in the photoreceptor and RPE layers. This backscatter is a mere 0.0001% (−60 dB) of the imaging light that enters the eye. The

weakest layer, the outer nuclear layer (ONL), is an additional 2.5 orders of magnitude dimmer (−85 dB).

The ideal imaging modality has the sensitivity to detect even the weakest of these reflections, enabling the cells that compose all retinal layers (neurons and neuroglial cells) to be seen.

2.3. Temporal Bandwidth (From Fastest to Slowest Cellular Change to Be Detected)

Vision involves millions of cells in the retina and brain and an enormity of biological processes (biochemical, diffusion, signaling, motility, circadian, growth, and death) that occur on vastly different timescales from microseconds to years. Some processes are of particular interest to vision scientists and clinicians. Arguably the most studied is the cascade of neuronal activities in the retina that is responsible for the first stages of visual function. These activities occur within a fraction of second, starting with light absorption and phototransduction by photoreceptors (initiated in milliseconds), followed by excitation of second-order neurons (tens of milliseconds), and ending with ganglion cell spike transmission to the brain (a couple of hundred milliseconds) (Rodieck 1998). Capturing this rapid cascade of events requires imaging systems with millisecond temporal resolution. Vascular dynamics are also of interest and increasingly important for assessing retinal health; observing them requires even higher (submillisecond) resolution. At the other extreme are processes that occur at much longer timescales and that have traditionally been of interest to clinicians, such as aging and disease progression; these are characterized by cell loss and remodeling that typically occur over years.

The ideal imaging modality captures all of these temporal dynamics, from microseconds to years. The wider is the range, the more useful is the method.

3. ADAPTIVE OPTICS OPTICAL COHERENCE TOMOGRAPHY IMAGING MODALITY

Of all the imaging modalities readily available to clinicians, OCT comes closest to the spatial resolution and sensitivity requirements needed for imaging transparent cells and their processes in the living human eye. Figure 2 illustrates the extent to which OCT satisfies these two requirements. As shown, clinical OCT's axial resolution (approximately 7 μm), lateral resolution (15 μm), and sensitivity (better than −90 dB) allow photograph-like image quality of all the major neural layers that compose the retina, including those that are highly transparent. However, magnifying a small section and comparing it to a same-scale histologic cross-section reveals that individual cells and cell-like structures are not discernible in clinical OCT images.

It was in this context that we and other groups sought to take advantage of OCT's strengths in axial resolution and sensitivity, while addressing its weaknesses in lateral resolution, temporal bandwidth (which is determined by image acquisition speed and image registration), and speckle noise. The latter is a high-contrast granular artifact that is ubiquitous in OCT images due to the interferometric nature of the method. In this section, we discuss how AO-OCT achieves substantial improvements over clinical OCT.

3.1. Adaptive Optics Improves Lateral Resolution

AO is used to improve lateral resolution by correcting dynamic ocular aberrations over a large dilated pupil (Liang et al. 1997). AO increases lateral resolution by roughly a factor of five over commercial OCT, permitting resolution of retinal details as small as 2–3 μm (see Figure 1a). AO also increases sensitivity because more reflected light can pass through the pupil and be captured by the AO-OCT system. The most common implementation of AO in AO-OCT systems has been with traditional wavefront sensors and correctors (Porter et al. 2006). While this hardware-based approach continues to be the gold standard, other approaches such as wavefront sensorless AO (no sensor) and computational AO (no sensor or corrector) have attracted attention as less expensive and more compact alternatives for use in AO-OCT (Wong et al. 2015, Hillmann et al. 2016a, Ginner et al. 2017).

3.2. High-Speed Imaging and Image Registration Reduces Eye Motion Artifacts

Separate from the temporal dynamics of the retinal tissue is the temporal dynamics of the entire eye, loosely referred to as eye motion, which impacts all ophthalmic imaging modalities. Subjects, even when visually fixating, exhibit continuous random movement of the retina, categorized as tremor, drift, and microsaccade, that occurs over timescales from milliseconds to seconds (Martinez-Conde et al. 2004). For single-cell imaging, the amplitude of the eye motion is many times larger than the cells to be imaged, which can result in substantial image blur and image warp depending on the speed at which the system acquires images. Thus, faster image acquisition and post-processing methods to correct blur and warp in the acquired images are critical to reduce motion artifacts.

We and others have found that increasing the image acquisition speed to at least 500,000 A-scans/s reduces motion artifacts by a large fraction (see Felberer et al. 2014, Kocaoglu et al. 2014b, Hillmann et al. 2016a, Azimipour et al. 2019a) (for definitions of A-scan and related OCT terms, see the sidebar titled Optical Coherence Tomography Image Terminology). Registering the acquired images corrects the remaining motion down to the level of individual en face strips (Kocaoglu et al. 2011b, 2014a; Azimipour et al. 2018), B-scans (Do 2016), or A-scans (K. Kurokawa, N. Do, J.A. Crowell, J. J. Lee & D.T. Miller, unpublished manuscript). Thus, with fast acquisition, we were able to register for the first time cells across images acquired at different time points with an accuracy much better than the size of single cells.

3.3. Image Averaging Reduces Speckle Noise and Improves Image Contrast

Speckle noise is a high-contrast granular artifact that is ubiquitous in OCT images of tissue due to interference between light scattered from the many organelles that compose the cells. The high contrast makes speckle a strongly deleterious artifact that masks cellular features that would otherwise be visible in the image. Particularly affected are transparent cells, whose weak signals result in extremely poor cell contrast compared to the high-contrast speckle noise, leading to failure to detect these cells even with sufficient resolution and sensitivity gained from AO-OCT.

Via simply averaging registered images acquired from the same retinal patch, speckle noise is reduced, while cell information is retained (Liu et al. 2016, 2017). We found empirically

that averaging a couple hundred registered AO-OCT volumes of the same retinal patch increased signal-to-noise ratio and image contrast, dramatically improving the clarity of individual cells, as is evident in the example of ganglion cell layer (GCL) somas in Figure 3. We attribute this improvement to organelle motion inside the cells that causes the speckle noise to change from image to image, while the cell structure remains constant from image to image. Thus, organelle motion acts as an intrinsic contrast agent.

3.4. Improving Temporal Bandwidth

We and others have found that a registered stack of AO-OCT volumes of the same retinal patch permits temporal evaluation of cellular processes (see Section 5). With image acquisition speeds of 500 KHz and higher (A-scan rate), dynamics from a fraction of a millisecond to over a year have been analyzed. This has required extensive development of post-processing algorithms based on temporal correlation (related to the algorithms used in OCT angiography) and phase-sensitive detection (e.g., measuring nanometer-scale axial displacements of the retinal reflection; see the sidebar titled Description of Optical Coherence Tomography).

3.5. Adaptive Optics Optical Coherence Tomography System Approaches

Many different types of AO-OCT systems have been developed over the past two decades, reflecting the many different OCT configurations to choose from. As described in the sidebar titled Optical Coherence Tomography Imaging Approaches, there are three broad categories of OCT, time-domain OCT (TD-OCT), spectral-domain OCT (SD-OCT), and swept-source OCT (SS-OCT), that can be realized with any of the three broad schemes of illumination and detection, point-scanning, line field, and full field (Drexler & Fujimoto 2015).

Hardware-based AO combined with point-scanning SD-OCT is the most mature AO-OCT configuration and has provided the best images to date of the cellular retina in humans. However, other AO and OCT implementations continue to be investigated as possible improvements over this gold standard. As used in humans, these include point-scanning SD-OCT with sensorless AO (Wong et al. 2015), point-scanning with computational AO combined with hardware-based AO (South et al. 2018), and line-scanning SD-OCT with computational AO (Ginner et al. 2017). AO combined with SS-OCT has also received considerable attention owing to its unprecedented multi-MHz A-scan rates. It has been implemented using point-scanning with hardware-based AO (Azimipour et al. 2019b) and full field with computational AO (Hillmann et al. 2016a). The former provides images of the retina that rival those obtained using point-scanning SD-OCT with hardware-based AO.

It remains unclear which AO-OCT configuration will ultimately perform best, if any. All of them have performance trade-offs among axial and lateral resolution, sensitivity, and image acquisition speed. At Indiana University, we have focused on point-scanning SD-OCT with hardware-based AO. It is with this configuration that most of the images in this review were obtained. The performance of this system is reasonably matched to the imaging requirements presented in Section 2. The system achieves a 3D resolution of $2.4 \times 2.4 \times 4.7$ μm^3 (width $\times$ width $\times$ depth) in retinal tissue, which allows essentially any cell in the retina

to be resolved, with the exception of, for example, very narrow cells such as cone photoreceptors at the foveal center. The system also provides phase-sensitive detection. This enables detection of extremely minute axial changes in tissue, some three orders of magnitude smaller than the system's axial resolution of 4.7 μm. This corresponds to a sensitivity of 5 nm, falling in the realm of molecules as depicted in Figure 1a. Because of OCT, we have the sensitivity to detect cellular reflections in any layer of the retina [from the RPE to the retinal nerve fiber layer (RNFL)]. High-speed image acquisition (at up to 1 MHz A-scan rate) coupled with image registration at the level of single A-scans and B-scans allows our system to track retinal dynamics from a fraction of a millisecond to over a year.

4. VISUALIZING TRANSPARENT CELLULAR-SCALE STRUCTURES

What should we expect retinal cells to look like in AO-OCT images? On first thought, we would hope that they mimic their characteristic appearances in histology acquired by light microscopy. However, the optical properties of tissue are vastly changed when removed from the eye and stained, and the imaging systems for AO-OCT and histology use and detect light in fundamentally different ways. Histological images also have notably better resolution. In most cases, we simply do not know what a given cell will look like in an AO-OCT image until we image it. From numerous studies, we know that some cell components appear similar in AO-OCT and histologic images (e.g., cell somas), while other cell components do not (e.g., photoreceptor segments, whose AO-OCT appearance is dominated by bright reflections at the segments' end tips). This disconnect often makes attribution of image features to the underlying anatomy difficult, especially for more finely detailed reflections. These are often interpreted with some uncertainty, occasional controversy, or even spirited debate (Spaide & Curcio 2011; Jonnal et al. 2014, 2015, 2017; Staurenghi et al. 2014; Litts et al. 2018; Cuenca et al. 2020). This iterative process is important, as misinterpretation can cause incorrect diagnosis and scientific conclusions.

With this caution about attribution made clear, we summarize many of the transparent retinal structures that we can now visualize and quantify with AO-OCT. These are divided into two groups by retinal depth: the photoreceptor–RPE–choriocapillaris (CC) complex, which contains photopigment and melanin that absorb light, and the inner retina, which is composed primarily of neurons (e.g., ganglion cells) that are nearly transparent, well index matched to surrounding cells, and tightly packed in three dimensions. Two illustrative averaged AO-OCT volumes are given in Figures 4 and 5; they were obtained by averaging approximately 2,200 and 1,300 volumes, respectively. Figure 4 shows a focused view of the outer retina, and Figure 5 shows a through-focus composite that preserves image sharpness over the full retinal thickness. These are some of the most detail-rich images that we know of in the living human retina and depict what can be achieved with state-of-the-art AO-OCT. Finally, we are compelled to add a third group, neuroglial cells, to our discussion. These cells occupy a good deal of the retina, yet we have had little success in identifying them in our images.

4.1 Photoreceptor-Retinal Pigment Epithelium-Choriocapillaris Complex

We can now visualize and quantify many of the cellular structures that compose the photoreceptor–RPE–CC complex using AO-OCT. These include the various components of cone photoreceptors, the rod photoreceptors, the RPE cell mosaic, and the anastomotic capillaries that make up the CC.

4.1.1. Cones.—The cone photoreceptor is the most-studied cell in the living human retina using AO imaging systems. Cones generate some of the strongest reflections in the retina and waveguide (funnel) light into their outer segments, thereby creating a high-contrast 2D pattern of the cone mosaic. This pattern is relatively easy to image with almost any AO imaging modality (Godara et al. 2010, Jonnal et al. 2016) and, under the right conditions, even without it (Miller et al. 1996, Potsaid et al. 2008, Pircher et al. 2011, LaRocca et al. 2016). The ubiquity of 2D cone mosaic images in the literature makes it easy to forget that cone cells actually extend over a significant fraction of the retinal thickness, from cone outer segment tips (COSTs) (which are ensheathed by RPE microvilli) to synaptic terminals in the outer plexiform layer (OPL). Thus, 2D cone mosaic images capture only a small portion of the cell structure.

Through the use of AO-OCT and OCT, cone cells have been found to generate an exceedingly wide range of reflectances, from their very bright reflections at the inner segment/outer segment junction (IS/OS) and COST, which form the cone mosaic image, to the extremely weak soma reflections, which are responsible for the dimmest band (ONL) in clinical OCT images. It is perhaps underappreciated that much of a cone cell is more transparent (less reflective) than the transparent neurons that compose the inner retinal layers.

Early AO-OCT users were the first to discover the bright IS/OS and COST reflections of individual cone cells and the prominent role that they played in forming the cone mosaic image (Zhang et al. 2006). Scientific studies followed into their optical and morphological properties, such as inner and outer segment lengths (Zawadzki et al. 2008, Wells-Gray et al. 2018b), ability to waveguide (capture) light (Felberer et al. 2014, Liu et al. 2015), relation to cone anatomy (Jonnal et al. 2014, 2017), and loss and alteration in diseases such as age-related macular degeneration (Wells-Gray et al. 2019) and glaucoma (Choi et al. 2011, Werner et al. 2011).

State-of-the-art AO-OCT permits much more appreciation of cone structure. We can identify most major cone components: inner segment, outer segment, soma, and axon (but not the synaptic terminal, whose high-spatial-frequency content cannot be resolved). The volume in Figure 4 and associated flythrough Supplemental Video 1 provide the best views of these components currently obtainable with our AO-OCT technology. Table 1 summarizes, by video frame number, our interpretation of the cone reflections. As an example from Table 1, our ability to measure subtle differences in the inner segment lengths of cone photoreceptors enables us to distinguish cones that are sensitive to short-wavelength (S) light from cones that are sensitive to medium- (M) and long-wavelength (L) light. S cones have slightly longer inner segments (Curcio et al. 1991) and consequently have IS/OS reflections that are shifted slightly deeper in the retina than that of M and L cones, as is evident in the two

IS/OS en face (C-scan) images in Figure 4 (labeled as "IS/OS: S cones" and "IS/OS: M and L cones") and the corresponding video (Supplemental Video 1). F. Zhang et al. (2019) independently confirmed these S cones based on their response to flashes of light with different spectra content (see Section 5.1). As another example from Table 1, the layer conventionally labeled as ONL in clinical OCT images is composed of two sublayers. The more basal sublayer contains photoreceptor somas, and the more apical one, referred to as Henle's fiber layer, contains photoreceptor axons (see Figure 2). With AO-OCT, these two sublayers of ONL can be differentiated based on cellular structural differences, as is evident in the two ONL en face images in Figure 4 (labeled as "ONL: somas" and "ONL: axons" and the corresponding video (Supplemental Video 1).

4.1.2. Rods.—Rod and cone photoreceptors share similar morphology, but rods have narrower and less reflective inner and outer segments that make them more challenging to image. In AO-OCT images, the rod's most characteristic and robust signal occurs at the rod outer segment tip (ROST), the site where the outer segment end tips are believed to embed into the anterior surface of RPE cells and create a dense granular ring of reflectance surrounding cone cells (see frames 88–90 in Supplemental Video 1). Thus, the ROST reflectance pattern can be thought of as a superposition of two photoreceptor mosaics, a coarse one that is dark and created by cone shadows and a bright one that is much finer and created by ROST reflections (Lee et al. 2013, Felberer et al. 2014, Liu et al. 2016).

Rod somas must be present in our AO-OCT images that show the ONL, but we have yet to identify them (presumably because of insufficient cell contrast and signal-to-noise ratio).

4.1.3. Retinal pigment epithelium.—RPE cells strongly reflect light at a level comparable to the bright reflections of the cone inner and outer segments. Unlike cone segments, however, individual RPE cells are difficult to discern. The problem is twofold: The bright reflections from the overlying photoreceptors obscure the RPE cells' spatial details, and RPE cells exhibit low internal contrast. AO-OCT avoids the first problem by using its micrometer-level axial resolution to section the narrow RPE band, removing the obscuring reflections of the photoreceptors (Torti et al. 2009, Felberer et al. 2014). Unfortunately, the low internal contrast of RPE cells is masked by speckle noise that creates a diffuse granular appearance and prevents delineation of these cells in single AO-OCT images. As described in Section 3, Liu et al. (2016,2019b) discovered that RPE cell contrast can be increased by averaging the registered RPE signal across time points (different AO-OCT images), sufficiently spaced (>5 s) that the natural motion of RPE cell organelles enhances cell contrast.

Following this protocol, the RPE mosaic in registered and averaged AO-OCT images appears as darkened spots in a brighter surround (see the RPE image in Figure 4 and frames 92–95 in the corresponding Supplemental Video 1). The darkened spots probably correspond to the cell nuclei. The large size of the nuclei ($\gg \lambda$) and their refractive index [$n \sim 1.4$ (Dunn et al. 1997)], similar to that of the surrounding cytoplasm [$n = 1.37$ (Dunn et al. 1997)], should facilitate highly anisotropic scatter. That is, incident light should be strongly scattered forward, with only weak backscattered light reaching the detector (Mourant et al. 1998). Consistent with this, we have observed that our AO-OCT beam penetrates readily

through the darkened spots to create a surreal polka-dot-like pattern of bright punctate reflections on the underlying choroidal vasculature (see Supplemental Figure 1). This pattern matches the arrangement of darkened spots in the RPE mosaic.

Attribution of the elevated reflection that surrounds the darkened spots remains speculative, but leading candidates include melanosomes and lipofuscin. In particular, melanin—which is synthesized and compartmentalized in melanosome organelles (Barral & Seabra 2004)—has a refractive index [$n = 1.7$ (Dunn et al. 1997)] that is notably higher than the cytoplasmic surround and is thus a likely source of reflected light. Consistent with this, several studies suggest that melanin is the primary source of the OCT signal in the RPE band (Baumann et al. 2012, Zhang et al. 2013, Wilk et al. 2017). The brightness of the surround and clarity of the RPE mosaic vary between subjects, suggesting differences in the concentration of one or more organelles that contribute to the RPE reflection. Clarity of the RPE mosaic is also generally reduced in older subjects. This reduction could be related to the loss of melanin and/or the increase in lipofuscin, both trends that occur with age (Feeney-Burns et al. 1984, Weiter et al. 1986). Other organelles may also contribute, including complex ones such as melanolysosomes and melanolipofuscin, which, like lipofuscin, increase with age (Feeney-Burns et al. 1984, Pollreisz et al. 2018); phagosomes, which are added daily to the RPE from outer segment disc shedding; and lysosomes and mitochondria, which are known to scatter significant light, although primarily at angles away from the eye's pupil (Wilson & Foster 2007, Wilson et al. 2007).

4.1.4.   Choriocapillaris.—The intricate network of anastomotic capillaries that compose the CC is arguably the most challenging structure of the photoreceptor–RPE–CC complex to image. The tight interconnections of this microvasculature necessitate high resolution, but more critically, the CC reflects little light, due primarily to the overlying RPE that blocks light from reaching it and contributes to its poor contrast. The spatial pattern of the CC is therefore not evident even in registered and averaged AO-OCT images (see Supplemental Figure 2e, left column). Kurokawa et al. (2012, 2017) found that AO-OCT in combination with temporal decorrelation methods used in OCT angiography dramatically improves vessel contrast by taking advantage of blood flow in the CC lumen (see Supplemental Figure 2e, right column). They used this angiographic method to measure key fundamental morphometric parameters of individual anastomotic capillaries (diameter, length, density, separation from RPE). We know of no other imaging method that can provide such detailed views of the anastomotic capillaries, including the many forms of OCT angiography (Braaf et al. 2013, Choi et al. 2013, Gorczynska et al. 2016, Migacz et al. 2019).

As demonstrated by other laboratories, AO-OCT angiographic methods also improve imaging of the major capillary beds of the retinal vasculature, which support the inner retina (Ju et al. 2017, Salas et al. 2017). Notable improvement in vessel sharpness and signal-to-noise ratio has been demonstrated compared to clinical OCT angiography, especially for the deeper plexus layers.

While AO-OCT angiography is effective for highlighting vasculature, the absence of similar types of motion in the other layers of the photoreceptor-RPE-CC complex preclude similar improvements. This is evident in Supplemental Figure 2c,d, which shows reflectance and

angiographic images of the Henle's fiber layer-ONL interface and IS/OS+COST projection. The striation pattern of photoreceptor axons and individual photoreceptors present in the reflectance images are absent in the angiographic images.

4.2. Inner Retinal Layers

We can now visualize and quantify numerous cellular structures of the inner retina using AO-OCT. These structures are presented by layer [GCL, inner plexiform layer (IPL), and inner nuclear layer (INL)], followed by a discussion on neuroglial cells, which reside throughout the layers.

4.2.1. Ganglion cell layer.—As suggested by the layer name, the GCL is packed tight with somas from ganglion cells. However, it also contains displaced amacrine cells, whose percent of the soma population increases from a couple of percent in the fovea, to 12–13% at the macula edge, and to nearly 80% in the far periphery (Curcio & Allen 1990). The ganglion cell has received considerable attention from the retinal imaging community, as it plays a fundamental role in processing visual signals prior to transmission to the brain. It is also the cell type primarily damaged by diseases of the optic nerve such as glaucoma (Quigley 1999, 2011; Weinreb et al. 2014; Fortune 2015), which is the leading cause of irreversible vision loss worldwide (Pascolini & Mariotti 2012). Like much of the inner retina, however, these neurons are extremely challenging to image owing to their near transparency, their similarity in refractive index to surrounding cells, and their tight packing. The examples that we present in Figures 3 and 5 demonstrate that state-of-the-art AO-OCT with image registration and averaging overcomes these problems. Averaging of images is critical. Without it, the contrast of GCL somas is typically half that of the image noise, making them indiscernible.

We can now capture substantial information about GCL somas and quantify their distinct morphometric properties in individual subjects. We observe that they are concentrated in a ring around the fovea and that their size and size variation increase with retinal eccentricity. We can also quantify GCL soma stack thickness, reflectance, density, and distribution of primary ganglion cell subtypes (parasol and midget ganglion cells) and the pooling of cone photoreceptor signals by ganglion cell dendritic fields across the macula (Liu et al. 2017). These spatial properties are of significant clinical interest because they are known to underlie various aspects of visual function.

GCL somas have also been visualized with AO-OCT by at least two other laboratories (Liu et al. 2018, Wells-Gray et al. 2018a). Our laboratory and theirs are attempting to measure changes in ganglion cell spatial properties as associated with aging (Kurokawa et al. 2019) and glaucoma (Wells-Gray et al. 2018a, Liu et al. 2019a, Jung et al. 2020). We discuss these topics further in Section 5.3.

We are also working to establish additional morphometric biomarkers (e.g., soma volume and internal reflections), to improve methods for differentiating soma types, and to extend our GCL soma analysis to displaced ganglion cells in the INL. Soma volume is of interest because it encapsulates key components of the protein and metabolic machinery necessary to maintain the cell's axon and thus has been proposed as an indicator of axon size (Watanabe

& Rodieck 1989). Liu et al. (2017) reported a statistically significant effect of GCL soma size on mean soma reflectance in four normal subjects, and we have since found it to be a general effect across subjects, with larger somas being generally more reflective than smaller ones (see Figure 6). We expect the reflectance pattern inside somas to contain clues about their organelle content. Improvements in AO-OCT imaging permit us to discern distinct patterns of bright punctate reflections internal to some of the larger somas in some images (see Figure 6), which we attribute to differences in the organelle composition of these cells. Because the soma organelle pattern is a better indicator of retinal cell type than soma size or density, individualized soma reflectance variations may offer additional insight into cell identity and help us better distinguish ganglion cell subtypes and differentiate them from displaced amacrine cells. We are currently investigating the collective power of these biomarkers to more accurately identify GCL soma subgroups.

There is also considerable interest in visualizing other principal components of ganglion cells, such as axons and dendritic branches. Ganglion cell axons form the RNFL, and their loss due to mechanical damage by the connective tissue of the optic disc is reported to be one of the earliest detectable glaucomatous changes (Quigley 2011, Fortune 2015). In several early AO-OCT studies, Zawadzki et al. (2007), Cense et al. (2009), and Torti et al. (2009) observed individual retinal nerve fiber bundles, and in a subsequent study, Kocaoglu et al. (2011a) measured the visibility and size distribution (width and thickness) of the bundles. However, all of these studies could not register and average many images, so bundle details at the spatial scale of axons were masked by high-contrast speckle noise. By registering and averaging, we found that AO-OCT images reveal bundles and axons as small as 3 μm, which is the caliber of a large ganglion cell axon (for size distribution, see the histologic studies by Ogden 1984, Wang et al. 2003). In the volume image of Supplemental Figure 3 and the corresponding Supplemental Video 3, individual retinal fiber bundles dissolve into an intricate, dense web of axon-like threads. Tracing these threads to their termination at underlying GCL somas would allow us to differentiate ganglion cell somas from displaced amacrine cells; the latter lack axons and are beyond our present capability to distinguish based on soma appearance. Unfortunately, the threads disappear as they arc downward, presumably because their reflections deviate away from the eye's pupil and thus escape our detection.

4.2.2. Inner plexiform layer.—Dense synaptic connections between axons of bipolar cells and dendrites of ganglion and amacrine cells compose the IPL. In AO-OCT en face images, these connections present as a uniform mesh of high-spatial-frequency irregularities with little apparent structure besides the occasional passing of a retinal vessel (Figure 5). However, the fine mesh appearance is not noise, as the IPL backscatters even more light than the GCL, whose somas we can readily observe. The cross-sectional view of the IPL may be more useful than its en face view. The IPL's unique stratification of synapses into sublamina of different depths anatomically segregates streams of information such as ON/OFF and parvo/magno within the visual pathway. We routinely observe this stratification in AO-OCT images—manifested as slight variations in reflectance—when the system is focused near the IPL depth. Representative B-scans in Supplemental Figure 4 show the spatial extent of the stratified bands (three hyper- and two hyporeflections), even where they deviate around

vessels that obstruct their path. Analysis of these B-scans shows that the spacing and reflectance difference between the maximum and minimum of the bands is approximately 6 μm and 1 dB, respectively. Imaging the IPL in this way presents a potentially powerful method to detect weak localized scatter changes that may be pathway dependent (e.g., ON versus OFF, cone versus rod) and may prove clinically useful. In addition, if disease processes differentially impact different pathways, then optical isolation at the IPL may serve as a novel diagnostic.

It is interesting to note that we know of only two other reports demonstrating the IPL hyper- and hyporeflective bands, and both were obtained with ultrahigh axial resolution OCT systems without AO. One used a broadband superluminescent diode (Tanna et al. 2010), and the other a visible light supercontinuum source (T. Zhang et al. 2019), to achieve the ultrahigh axial resolution.

4.2.3. Inner nuclear layer.—AO-OCT investigation of the cellular details of the INL is just beginning. The INL reflects less light than the layers above it (IPL, GCL, and RNFL), which would seem to suggest less cellular content. On the contrary, it contains a panoply of densely packed somas, principally amacrine, bipolar, Müller, and horizontal cells, along with a scattering of displaced ganglion and interplexiform cells. Histology indicates that the INL is coarsely stratified, with amacrine, displaced ganglion, and interplexiform cells in the inner sublayer adjoining the IPL, Muller cells in the middle sublayer, horizontal cells in the outer sublayer adjoining the OPL, and bipolar cells in all sublayers (Hogan et al. 1971). Given this stratification, our observations of cellular structure across the entire INL thickness imply that we are detecting many of these different types of cells.

The most prominent cell-like structure that we see in the INL is a bright, large soma-like body that sparsely populates the inner sublayer (see Figure 5 and frames 53–64 of Supplemental Video 2). These soma-like bodies reflect more light than surrounding cells and are of the size (approximately 18 μm) expected of large ganglion cell somas. We routinely find these structures whenever focus is placed near the INL-IPL interface. We speculate that they may be ganglion cells that are displaced from their normal location in the GCL and that represent a small percentage of the total ganglion cell population (Bunt & Minckler 1977). They could also be large interplexiform cells, but interplexiform cell somas are reported to be smaller (11 μm) (Kolb et al. 1992). Interestingly, as shown in Figure 5, many of these bright, large soma-like bodies are notably larger than the overlying GCL somas of the same volume image (approximately 12 μm). Unfortunately, little is known about displaced ganglion cells compared to their population in the GCL, especially in humans, and even less is known about interplexiform cells.

The most numerous cell-like structure that we see in the INL is a faint, small soma-like body approximately 6 to 9 μm in diameter. These structures tightly pack and permeate the entire INL thickness. Their size and distribution are suggestive of bipolar somas, which are the most numerous cells in the INL. Bipolar soma size in human and macaque varies in the literature, but is typically reported to be 6–7 μm (Crooks & Kolb 1992, Haverkamp et al. 2003, Joo et al. 2011). Their density of 40,000–60,000 somas/mm^2 is higher than that of the

overlying ganglion cells, even where ganglion cells concentrate in a ring around the fovea (Lei et al. 2011).

4.3. Neuroglial Cells

Neuroglial cells provide structural and metabolic support of the retinal neurons, with major types including Müller cells, microglial cells, and astrocytes. While our effort has focused on identifying the neurons in the visual pathway, we have had little success in identifying neuroglial cells. Perhaps most surprising is our lack of evidence of Müller cells, given that they stretch across most of the retinal thickness and are some of the largest cells to occupy the retina. Müller cells have also been reported to waveguide light down to the photoreceptors (Franze et al. 2007), which, if true, should make them easier to observe in our images, i.e., they would appear dark on a bright surround when viewed in en face owing to their high transmission. Müller cell somas reside in the INL; as we observe somas in this layer, we may well see them in our images but not identify them as such. We have also yet to identify microglial and astrocyte cells. Surely these cells are present in our images, but recognition of them is likely hampered by their ability to morph into the space between neurons, thus taking on nondistinct and irregular forms.

Following Liu et al. (2017, 2018), Kurokawa et al. (2020) observed macrophage-like cells, a group of neuroglial cells, moving on the surface of the inner limiting membrane and speculated that these are hyalocytes, which share a common origin with microglial cells. These cells are discussed in Section 5.3.3. Aside from this cell type, however, much work remains to identify and characterize neuroglial cells in AO-OCT images.

5. VISUALIZING TRANSPARENT CELLULAR-SCALE PROCESSES

In this section, we summarize many of the processes in retinal cells that we can now visualize and quantify with AO-OCT. These are arranged into three groups (those in photoreceptors, RPE cells, and inner retinal cells), and they cover a wide range of temporal scales (milliseconds, seconds, minutes, days, and years). Some of the processes studied involve photostimulation. Because photoreceptors have been the primary focus of AO-OCT studies, our coverage reflects this disproportion.

5.1. Photoreceptors

Our understanding of how physiological information is encoded in photoreceptor reflections has grown considerably since the first images of single cones were captured in the living human retina almost 25 years ago (Miller et al. 1996). With AO-OCT, we have discovered the optical signatures of outer segment disc shedding (Kocaoglu et al. 2016, F. Zhang et al. 2017) and renewal (Jonnal et al. 2010, 2012; F. Zhang et al. 2017) and portions of the phototransduction process and its downstream effects (Hillmann et al. 2016b, Azimipour et al. 2019b, F. Zhang et al. 2019). Today's AO-OCT can track photoreceptor dynamics faster than a millisecond (e.g., early events of phototransduction), as well as extremely slow processes (e.g., disc shedding and renewal) that evolve over an entire day or longer. The capability of AO-OCT to detect minute axial displacements of the photoreceptor's

reflections is critical for detecting these processes (see the sidebar titled Measuring Changes in the Cone Outer Segment Length).

5.1.1. Cone outer segment disc shedding and renewal.—Photoreceptor outer segments undergo daily renewal and shedding of their membranous discs to prevent damage from the accumulation of light-induced photo-oxidative compounds (Young 1967, Young & Bok 1969, Steinberg et al. 1977, Anderson et al. 1978). Renewal is the continual assembly of new membranous discs at the end of the outer segment proximal to the inner segment, which elongates the outer segment by a couple of microns each day. This new growth is offset by shedding, a discrete, diurnal event in which small packets of discs are pruned from the distal end of the outer segment. These physiological processes help maintain photoreceptor health, and their dysfunction is associated with numerous retinal diseases, including age-related macular degeneration and retinitis pigmentosa (Kevany & Palczewski 2010, Ruggiero & Finnemann 2014). Much is known about these processes based on extensive studies in animal models in postmortem eyes. However, how these translate to the living retina and humans—where this knowledge can make its largest impact for improved diagnosis and therapeutics—have been major obstacles. Only recently have these processes been directly detected in the living human eye.

With AO-OCT, we have found that the optical signature of disc shedding is an abrupt transient loss in the COST reflection mentioned above, followed by its return minutes later slightly closer to the IS/OS reflection, indicating a shorter outer segment length (Kocaoglu et al. 2016). Loss in outer segment length is approximately 2 μm, consistent with the histological observation of pruning of a small packet of discs.

In contrast to outer segment shedding, the extremely slow elongation of the outer segment caused by renewal (approximately 0.08 μm/hr) results in a magnitude change that is more difficult to detect. We have developed two distinct strategies for improving precision. The first takes advantage of the statistical power that accrues from tracking thousands of individual cones in the same retinal patch over hundreds of time points across the day, measuring their outer segment lengths, and then pooling their measurements. A recent study by F. Zhang et al. (2017; see also Zhang 2019) showed that this method increased AO-OCT precision approximately 40-fold, allowing detection of outer segment length changes as small as 10 nm. However, measurements are limited to aggregate changes, not those of individual photoreceptors.

The second strategy uses the phase information contained in reflections (as measured by OCT) to measure local changes in optical path length (OPL). Through measurement of the phase difference between the IS/OS and COST reflections of a single photoreceptor, the outer segment is converted into a biological interferometer with exquisite sensitivity to small ($\ll \lambda$) changes in outer segment length. This strategy is immune to the effects of axial eye motion, as the IS/OS and COST reflections experience the exact same motion. The strategy was first applied using AO flood illumination, achieving an outer segment length sensitivity of 139 nm (Jonnal et al. 2010), and then using AO-OCT, achieving an outer segment length sensitivity of 45 nm (Jonnal et al. 2012).

We have used both strategies, while also monitoring the disappearance of COST, to measure outer segment renewal and shedding in thousands of individual cones tracked across the entire day. We now know that human cones shed in a diurnal rhythm with a burst shortly after light onset, and that this rhythm is predominately regulated by light exposure rather than circadian control (Zhang 2019; F. Zhang, K. Kurokawa & D.T. Miller, unpublished manuscript). We find that most cones shed once a day, with a small fraction shedding multiple times a day and a few not shedding at all. In contrast, the outer segment is renewed at a constant rate of approximately 0.08 μm/hr regardless of light exposure, which is equivalent to the generation of approximately 3 new outer segment discs per hour.

5.1.2. *OPL* cone response to photostimulation.—It was recently discovered that light stimulation of cone photoreceptors also generates a change in the optical path length of the cone outer segment, but on a much faster timescale than that of outer segment renewal (fractions of a second instead of hours). These photostimulation-induced changes have been investigated by several groups using a variety of phase-sensitive AO-OCT methods: (*a*) full-field OCT with computational aberration correction at 840 nm (Hillmann et al. 2016b), (*b*) AO SS-OCT at 1,063 nm (Azimipour et al. 2019b), and (*c*) AO SD-OCT at 790 nm (F. Zhang et al. 2019). These methods achieve outer segment length sensitivity as small as 5 nm, just one-fifth the spacing of the outer segment membrane discs. As illustrated in Figure 7b, two distinct dynamics in the cone *OPL* are revealed by these systems. First is an initial decrease that is brief (milliseconds), is small (tens of nanometers), and varies linearly with accumulated flash energy and predicted level of photopigment bleaching. This is followed by a second dynamic whose increase is much longer (seconds), is larger (hundreds of nanometers), and varies nonlinearly with accumulated flash energy and predicted level of photopigment bleaching.

The timescale and linear behavior of the fast *OPL* response are consistent with the photoactivation of photopigment molecules. This is the first step of the phototransduction cascade; it occurs within approximately 0.5 ms of photon absorption and is linearly proportional to bleach level (Rodieck 1998). The slow phase of the response is easier to detect but harder to attribute. Maximum *OPL* (approximately 0.5% of outer segment length) occurs about half a second after the flash, a duration longer than activation and deactivation of phototransduction combined (Schnapf et al. 1990). This maximum phase change is therefore probably dominated by indirect effects of transduction, such as the osmotic swelling of the outer segment hypothesized byJonnal et al. (2007) and supported by observations made using conventional OCT images in rods of wild-type and knockout mice (P. Zhang et al. 2017).

5.1.3. Applications of the *OPL* cone response to photostimulation.—We are just starting to understand the relationship between *OPL* and vision in both normal and diseased eyes. For example, the different spectral types of cones (S, M, and L) respond differently in *OPL* to the same light flash, allowing cones to be classified by types that can then be mapped (Figure 7). This technique is orders of magnitude faster and more accurate than prior approaches such as AO retinal densitometry (Roorda & Williams 1999, Sabesan et al. 2015), promising application of in vivo cone classification to a much wider range of color

vision applications. For example, in the past year, we have used AO-OCT to classify cones into spectral types in as many subjects ($n = 16$) as have been studied over the past two decades with AO retinal densitometry ($n = 15$).

This same technique is also being used to reveal how color vision performance (phenotype) and genetics are manifested in single cones. We find three spectral types of cones in color-normal subjects and two types in dichromats. We are also finding more subtle distinctions in deuteranomalous subjects; for example, there is evidence of multiple types of L-cone opsin that present with slightly different spectral sensitivities (Zhang 2019; F. Zhang, K. Kurokawa, M.T. Bernucci, H.W. Jung, A. Lassoued, J.A. Crowell, et al., unpublished manuscript).

The *OPL* response of the cone outer segment to light may also offer greater clinical utility than structural measurements of cones such as cone density, spacing, and layer thickness. This is because *OPL* is a measure of function that is more directly related to cell physiology and health. For example, based on the *OPL* response, we found that cone function decreases with the degree of retinitis pigmentosa severity. In these diseased eyes, many cone cells of the same retinal patch responded more or less similarly to the same light flash, but clear differences were apparent, with some cones more affected by the disease than others. We were also struck by how disconnected the structural appearance of a cone cell could be from its response to light. Many cones that appeared structurally normal had diminished responses, some dramatically (Lassoued et al. 2020; A. Lassoued, F. Zhang, K. Kurokawa, J.A Crowell & D.T. Miller, unpublished manuscript).

5.1.4. Other types of photoreceptor responses to photostimulation.—Optical changes of cones in response to photostimulation are not limited to the optical path length of the outer segment. Azimipour et al. (2019b) reported (*a*) changes in IS/OS reflectivity; (*b*) the appearance and/or movement of an extra hyperband between IS/OS and COST; and (*c*) change in the space distal to COST, including the subretinal space and RPE. *OPL* changes have also been found in rod outer segments in our laboratory and those of Gereon Huttmann (Pfäffle et al. 2019) and Ravi Jonnal (Azimipour et al. 2020). The similarity of these changes to those in cones suggests that outer segment expansion may be a universal consequence of photoreceptor activation regardless of cell type.

5.2. Retinal Pigment Epithelium

RPE cells lack the pristine phase signal of cone outer segments, i.e., the *OPL* between the IS/OS and COST reflections. Instead, the RPE reflection is dominated by speckle noise, generated by the optical interference of light scattered from the many organelles that compose the cells and gives the reflection a granular appearance. Each speckle (granule) has its own unique random phase. As discussed in Section 4, the intrinsic motion of organelles causes AO-OCT volumes acquired at different times to exhibit different speckle patterns. Averaging multiple volumes suppresses the speckle and reveals the RPE cell mosaic (Liu et al. 2016, 2019b). However, the change in speckle may itself contain vital information about RPE cell physiology (Futter 2006) that is lost by averaging.

To investigate, Liu et al. (2019b) quantified RPE speckle field dynamics in terms of an exponential decay time constant (τ), the time for organelle motility to decorrelate the amplitude of the speckle field across the interiors of individual RPE cells. They found τ to vary with depth in the cell, with the basal side being more dynamic (smaller τ) than the apical side and middle. Mean τ was approximately 5 s (see Figure 8).

It is unclear which organelles contribute to the motility signal embodied in the changing speckle field, but leading candidates include melanosomes, phagosomes, and lipofuscin, with other possible contributors being melanolysosomes, melanolipofuscin, lysosomes, and mitochondria.

Melanosomes and phagosomes are known for their motility (Futter 2006). Variation in the concentrations of melanosomes and lipofuscin across the RPE depth (Weiter et al. 1986, Pollreisz et al. 2018) may contribute to the differences in τ that we measure. These concentrations also change with age. Melanosome numbers decrease, while lipofuscin accumulates as a byproduct of phagocytosis of photoreceptor outer segments (Freeney-Burns et al. 1984, Weiter et al. 1986). These changes presumably affect the cell's motility in a manner detectable by AO-OCT. Establishing a normative baseline for the motility dynamics will allow us to compare dynamics in retinal diseases that afflict the RPE. Abnormal transport of phagosomes (Gibbs et al. 2003, Jiang et al. 2015) and interrupted melanosome movement (Gibbs et al. 2004) in mutant RPE cells have been suggested as sources of RPE motility change that are directly linked to RPE function deficits found in many retinal diseases.

5.3. Inner Retina

There are few reports on cellular-level dynamics of neurons in the inner retina of humans. Inner retinal dynamics are difficult to measure because they induce small changes in an already weak reflection that is dominated by speckle noise. In this section, we summarize key results from two recent papers. The papers look at fast dynamics (over seconds or less), one with and the other without photostimulation. One of the two papers also shows slower dynamics that occur over both minutes and one year.

5.3.1. Fast dynamics without photostimulation.—Kurokawa et al. (2020) measured the temporal dynamics of individual retinal layers (RNFL, GCL, and IPL) and specific tissue types within those layers using a temporal autocorrelation method developed for AO-OCT images. They found the speckle field amplitude of the layers to decorrelate within approximately 1 s. However, significant differences existed between the layers: The GCL was the most dynamic, approximately 30% faster than the RNFL and IPL. Most intriguingly, the dynamics of individual GCL somas varied appreciably between cells. Figure 9 illustrates the spread, showing the distribution of soma activity in GCL patches from two subjects. The approximately threefold difference between the least and most active GCL somas (approximately 0.4 to 1.2 s) is notably larger than the 95% confidence interval of the measurement, indicating that the method can reliably detect differences in activity between individual somas. This technique may support development of physiologically

sensitive biomarkers for ganglion cell health because the measured activity relates directly to soma physiology.

5.3.2. Fast dynamics with photostimulation.—Our success at detecting *OPL* in photostimulated photoreceptors motivated the search for similar changes in the inner retina. We repeated the previously described experiment measuring temporal autocorrelation in the inner retina, but with photostimulation. To our surprise, we observed no effect of stimulation under any condition (different spectra, intensities, and flicker rates). The normal motility of organelles internal to these cells may have masked any additional effect of cell excitation, or the cells' organelle motilities may not be affected by cell excitation.

Pfäffle et al. (2019) pursued a different strategy, measuring *OPL* between the GCL and IPL layers using full-field OCT with computational aberration correction. Using continuous white light exposure, they observed that the GCL–IPL optical path length increased, as did the cone outer segment; however, the increase was slower (over seconds), and its amplitude was an order of magnitude smaller (40 nm instead of 300 nm), than those of the outer segment. The authors speculated that the slower response derives from osmotic-driven water flux rather than direct neuronal function; it also does not follow the time course expected of hemodynamic changes. Most remarkably, they observed the GCL-IPL response to be spatially shifted and warped relative to the patch of photoreceptors stimulated (Figure 10), in a manner consistent with the anatomical projection of cone photoreceptors onto ganglion cells (Drasdo et al. 2007).

5.3.3. Slow dynamics over minutes and a year.—Cellular dynamics on other timescales must be present in the retina. However, we know of only one study using AO-OCT that has analyzed cellular changes on longer timescales in the inner retina (Kurokawa et al. 2020).

5.3.3.1. Dynamics over minutes.: Dynamics over minutes were measured using time-lapse imaging and a temporal speckle contrast method related to that used in OCT angiography but adapted for the longer timescale. Our most notable observation was the movement of macrophage-like cells—bright, irregular, star-shaped cells that sparsely cover the surface of the inner limiting membrane (ILM) (see in an en face view of macrophage-like cells in Supplemental Figures 3 and 5 and Supplemental Video 3). We detected the micron-scale motion of the processes of these cells as they probed their local microenvironment. Based on the cells' few stout processes and their apparent random distribution in a narrow region just anterior of the ILM, we speculated that these cells are hyalocytes, a subtype of macrophage-like cell that typically resides in the cortical vitreous either adjacent to or abutting on the retinal surface (see Lazarus & Hageman 1994). Monitoring of these cells may prove clinically useful, as hyalocytes have been implicated in the pathogenesis of numerous retinal diseases, and their numbers are believed to fluctuate as a function of retinal health (Vagaja et al. 2012).

5.3.3.2. Dynamics over a year.: We have previously demonstrated the ability to track individual GCL somas over minutes and to measure their key morphological properties. This capability raises the question of whether we can track GCL somas across much longer

intervals with sufficient accuracy to measure changes in these cells, a key one being loss. We know ganglion cells are lost every year during progression of glaucoma [e.g., 5%/year (Medeiros et al. 2012, Hirooka et al. 2016)] and other neurodegenerative disorders such as Alzheimer's disease (Berisha et al. 2007), Parkinson's disease (Archibald et al. 2009), and amyotrophic lateral sclerosis (Volpe et al. 2015). Even in subjects free of ocular disease, a small fraction of these cells die each year as part of normal aging (0.19–0.72%/year) (Gao & Hollyfield 1992, Curcio & Drucker 1993, Blanks et al. 1996, Harman et al. 2000, Lei et al. 2011). Thus, there is a major clinical need to differentiate loss due to disease from that due to aging as early as possible to intervene with appropriate treatment to minimize cell death.

Kurokawa et al. (2020) tested the feasibility of measuring ganglion cell loss over a one-year interval. This involved registering images of the same patch of GCL somas acquired one year apart and then visually inspecting these image pairs in rapid alternation. Supplemental Figure 5 shows a representative example in which a single cell disappeared over the one-year interval. In this GCL patch, we identified 590 somas that were present at both ends of the interval. The missing soma is more salient in a magnified view in Supplemental Figure 5d,h, which also reveals migration of neighboring somas into the void created by the vanished soma (representing a form of retinal remodeling at the cellular level). Loss of 1 out of 590 GCL neurons is consistent with histologic reports of aging-related loss and within the range of loss rates (0.15 ± 0.04%/year) that Kurokawa et al. (2019) measured in an ongoing AO-OCT longitudinal study of normal subjects. In general, Kurokawa et al. found GCL soma losses to be rare, isolated events. The ability of their method to detect these single loss events demonstrates the potential for extremely early detection of the onset of ganglion cell-affecting diseases such as glaucoma.

6. CONCLUSION

AO-OCT performance has improved dramatically over the past few years, making it a powerful tool for studying the cellular details of the living human retina. The volume images that we acquire today are packed full with structural and physiological details, many of which still await study and interpretation. With these images, AO-OCT is leading to discoveries about how cells operate in the living human eye, allowing us to test against animal models and histology. In doing so, AO-OCT is supplanting prior state-of-the-art imaging methods and is moving closer to clinical fruition. The ability to measure a wide range of physiological processes, from fast ones like phototransduction to extremely slow ones like cell death and remodeling, demonstrates that this technology will change the way diseases of the eye are studied, diagnosed, and monitored. It remains to be seen how far AO-OCT can take us into the cellular space of the retina before another paradigm-shifting technology is needed for the next performance leap.

Supplementary Material

Refer to Web version on PubMed Central for supplementary material.

ACKNOWLEDGMENTS

LITERATURE CITED

Anderson DH, Fisher SK, Steinberg RH. 1978 Mammalian cones: disc shedding, phagocytosis, and renewal. Investig. Ophthalmol. Vis. Sci 17(2):117–33 [PubMed: 415019]

Archibald NK, Clarke MP, Mosimann UP, Burn DJ. 2009 The retina in Parkinson's disease. Brain 132(5):1128–45 [PubMed: 19336464]

Azimipour M, Jonnal RS, Werner JS, Zawadzki RJ. 2019a Coextensive synchronized SLO-OCT with adaptive optics for human retinal imaging. Opt. Lett 44(17):4219–22 [PubMed: 31465366]

Azimipour M, Migacz JV, Zawadzki RJ, Werner JS, Jonnal RS. 2019b Functional retinal imaging using adaptive optics swept-source OCT at 1.6 MHz. Optica 6(3):300–3 [PubMed: 33511257]

Azimipour M, Valente D, Vienola KV, Werner JS, Zawadzki RJ, Jonnal RS. 2020 Investigating the functional response of human cones and rods with a combined adaptive optics SLO-OCT system. Proc. SPIE 11218:1121813

Azimipour M, Zawadzki RJ, Gorczynska I, Migacz J, Werner JS, Jonnal RS. 2018 Intraframe motion correction for raster-scanned adaptive optics images using strip-based cross-correlation lag biases. PLOS ONE 13(10):e0206052 [PubMed: 30359401]

Barral DC, Seabra MC. 2004 The melanosome as a model to study organelle motility in mammals. Pigment Cell Res. 17(2):111–18 [PubMed: 15016299]

Baumann B, Baumann SO, Konegger T, Pircher M, Götzinger E, et al. 2012 Polarization sensitive optical coherence tomography of melanin provides intrinsic contrast based on depolarization. Biomed. Opt. Express 3(7):1670–83 [PubMed: 22808437]

Berisha F, Feke GT, Trempe CL, McMeel JW, Schepens CL. 2007 Retinal abnormalities in early Alzheimer's disease. Investig. Ophthalmol. Vis. Sci 48(5):2285–89 [PubMed: 17460292]

Blanks JC, Torigoe Y, Hinton DR, Blanks RH. 1996 Retinal pathology in Alzheimer's disease. I. Ganglion cell loss in foveal/parafoveal retina. Neurobiol. Aging 17(3):377–84 [PubMed: 8725899]

Boycott BB, Dowling JE, Kolb H. 1969 Organization of the primate retina: light microscopy, with an appendix: a second type of midget bipolar cell in the primate retina. Philos. Trans. R. Soc. Lond. B 255(799):109–84

Braaf B, Vienola KV, Sheehy CK, Yang Q, Vermeer KA, et al. 2013 Real-time eye motion correction in phase-resolved OCT angiography with tracking SLO. Biomed. Opt. Express 4(1):51–65 [PubMed: 23304647]

Bunt AH, Minckler DS. 1977 Displaced ganglion cells in the retina of the monkey. Investig. Ophthalmol. Vis. Sci 16(1):95–98 [PubMed: 401780]

Burns SA, Elsner AE, Sapoznik KA, Warner RL, Gast TJ. 2018 Adaptive optics imaging of the human retina. Prog. Retin. Eye Res 62(1):60–65

Cense AJ, Koperda E, Brown JM, Kocaoglu OP, Gao W, et al.2009 Volumetric retinal imaging with ultrahigh-resolution spectral-domain optical coherence tomography and adaptive optics using two broadband light sources. Opt. Express 17(5):4095–111 [PubMed: 19259249]

Chen X, Hou P, Jin C, Zhu W, Luo X, et al. 2013 Quantitative analysis of retinal layer optical intensities on three-dimensional optical coherence tomography. Investig. Ophthalmol. Vis. Sci 54(10):6846–51 [PubMed: 24045992]

Choi SS, Zawadzki RJ, Lim MC, Brandt JD, Keltner JL, et al. 2011 Evidence of outer retinal changes in glaucoma patients as revealed by ultrahigh-resolution in vivo retinal imaging. Br. J. Ophthalmol 95(1):131–41 [PubMed: 20956277]

Choi W, Mohler KJ, Potsaid B, Lu CD, Liu JJ, et al. 2013 Choriocapillaris and choroidal microvasculature imaging with ultrahigh speed OCT angiography. PLOS ONE 8(12):e81499 [PubMed: 24349078]

Chui TYP, VanNasdale DA, Burns SA. 2012 The use of forward scatter to improve retinal vascular imaging with an adaptive optics scanning laser ophthalmoscope. Biomed. Opt. Express 3(10):2537–49 [PubMed: 23082294]

Cole ED, Novais EA, Louzada RN, Waheed NK. 2016 Contemporary retinal imaging techniques in diabetic retinopathy: a review. Clin. Exp. Ophthalmol 44(4):289–99 [PubMed: 26841250]

Crooks J, Kolb H. 1992 Localization of GABA, glycine, glutamate and tyrosine hydroxylase in the human retina. J. Comp. Neurol 315(3):287–302 [PubMed: 1346792]

Cuenca N, Ortuño-Lizarán I, Sánchez-Sáez X, Kutsyr O, Albertos-Arranz H, et al. 2020 Interpretation of OCT and OCTA images from a histological approach: clinical and experimental implications. Prog. Retin. Eye Res. In press

Curcio CA, Allen KA. 1990 Topography of ganglion cells in human retina. J. Comp. Neurol 300(1):5–25 [PubMed: 2229487]

Curcio CA, Allen KA, Sloan KR, Lerea CL, Hurley JB, et al. 1991 Distribution and morphology of human cone photoreceptors stained with anti-blue opsin. J. Comp. Neurol 312(4):610–24 [PubMed: 1722224]

Curcio CA, Drucker DN. 1993 Retinal ganglion cells in Alzheimer's disease and aging. Ann. Neurol 33(3):248–57 [PubMed: 8498808]

Delori FC, Pflibsen KP. 1989 Spectral reflectance of the human ocular fundus. Appl. Opt 28(6):1061–77 [PubMed: 20548621]

Do N 2016 Parallel processing for adaptive optics optical coherence tomography (AO-OCT) image registration using GPU. MS thesis, Indiana Univ./Purdue Univ, Indianapolis

Dong ZM, Wollstein G, Wang B, Schuman JS. 2017 Adaptive optics optical coherence tomography in glaucoma. Prog. Retin. Eye Res 57:76–88 [PubMed: 27916682]

Drasdo N, Millican CL, Katholi CR, Curcio CA. 2007 The length of Henle fibers in the human retina and a model of ganglion receptive field density in the visual field. Vis. Res 47(22):2901–11 [PubMed: 17320143]

Drexler W, Fujimoto JG, eds. 2015 Optical Coherence Tomography: Technology and Applications. Berlin: Springer 2nd ed.

Dunn AK, Smithpeter CL, Welch AJ, Richards-Kortum RR. 1997 Finite-difference time-domain simulation of light scattering from single cells. J. Biomed. Opt 2(3):262–66 [PubMed: 23014912]

Feeney-Burns L, Hilderbrand ES, Eldridge S. 1984 Aging human RPE: morphometric analysis of macular, equatorial, and peripheral cells. Investig. Ophthalmol. Vis. Sci 25(2):195–200 [PubMed: 6698741]

Felberer F, Kroisamer J-S, Baumann B, Zotter S, Schmidt-Erfurth U, et al. 2014 Adaptive optics SLO/OCT for 3D imaging of human photoreceptors in vivo. Biomed. Opt. Express 5(2):439–56 [PubMed: 24575339]

Fortune B 2015 In vivo imaging methods to assess glaucomatous optic neuropathy. Exp. Eye Res 141:139–53 [PubMed: 26048475]

Franze K, Grosche J, Skatchkov SN, Schinkinger S, Foja C, et al. 2007 Muller cells are living optical fibers in the vertebrate retina. PNAS 104(20):8287–92 [PubMed: 17485670]

Futter CE. 2006 The molecular regulation of organelle transport in mammalian retinal pigment epithelial cells. Pigment Cell Res. 19(2):104–11 [PubMed: 16524426]

Gao H, Hollyfield JG. 1992 Aging of the human retina. Differential loss of neurons and retinal pigment epithelial cells. Investig. Ophthalmol. Vis. Sci 33(1):1–17 [PubMed: 1730530]

Gao W, Cense AJ, Zhang Y, Jonnal RS, Miller DT. 2008 Measuring retinal contributions to the optical Stiles-Crawford effect with optical coherence tomography. Opt. Express 16(9):6486–501 [PubMed: 18516251]

Georgiou M, Kalitzeos A, Patterson EJ, Dubra A, Carroll J, Michaelides M. 2018 Adaptive optics imaging of inherited retinal diseases. Br. J. Ophthalmol 102(8):1028–35 [PubMed: 29141905]

Gibbs D, Azarian SM, Lillo C, Kitamoto J, Klomp AE, et al. 2004 Role of myosin VIIa and Rab27a in the motility and localization of RPE melanosomes. J. Cell Sci 117(26):6473–83 [PubMed: 15572405]

Gibbs D, Kitamoto J, Williams DS. 2003Abnormal phagocytosis by retinal pigmented epithelium that lacks myosin VIIa, the Usher syndrome 1B protein. PNAS 100(11):6481–86 [PubMed: 12743369]

Gill JS, Moosajee M, Dubis AM. 2019 Cellular imaging of inherited retinal diseases using adaptive optics. Eye 33:1683–98 [PubMed: 31164730]

Ginner L, Kumar A, Fechtig D, Wurster LM, Salas M, et al. 2017 Noniterative digital aberration correction for cellular resolution retinal optical coherence tomography in vivo. Optica 4(8):924–31

Godara P, Dubis AM, Roorda AJ, Duncan JL, Carroll J. 2010 Adaptive optics retinal imaging: emerging clinical applications. Optom. Vis. Sci 87(12):930–41 [PubMed: 21057346]

Gorczynska I, Migacz JV, Zawadzki RJ, Capps AG, Werner JS. 2016 Comparison of amplitude-decorrelation, speckle-variance and phase-variance OCT angiography methods for imaging the human retina and choroid. Biomed. Opt. Express 7(3):911–42 [PubMed: 27231598]

Harman A, Abrahams B, Moore S, Hoskins R. 2000 Neuronal density in the human retinal ganglion cell layer from 16–77 years. Anat. Rec 260(2):124–31 [PubMed: 10993949]

Haverkamp S, Haeseleer F, Hendrickson A. 2003 A comparison of immunocytochemical markers to identify bipolar cell types in human and monkey retina. Vis. Neurosci 20(6):589–600 [PubMed: 15088712]

Hermann B, Fernández EJ, Unterhuber A, Sattmann H, Fercher AF, et al. 2004 Adaptive-optics ultrahigh-resolution optical coherence tomography. Opt. Lett 29(18):2142–44 [PubMed: 15460883]

Hillmann D, Spahr H, Hain C, Sudkamp H, Franke G, et al. 2016a Aberration-free volumetric high-speed imaging of in vivo retina. Sci. Rep 6(7):35209 [PubMed: 27762314]

Hillmann D, Spahr H, Pfäffle C, Sudkamp H, Franke G, Hüttmann G. 2016b In vivo optical imaging of physiological responses to photostimulation in human photoreceptors. PNAS 113(46):13138–43 [PubMed: 27729536]

Hirooka K, Izumibata S, Ukegawa K, Nitta E, Tsujikawa A. 2016 Estimating the rate of retinal ganglion cell loss to detect glaucoma progression: an observational cohort study. Medicine 95(30):e4209 [PubMed: 27472691]

Hogan MJ, Alvarado JA, Weddell JE. 1971 Histology of the Human Eye. Philadelphia: W.B. Saunders

Huang D, Swanson EA, Lin CP, Schuman JS, Stinson WG, et al. 1991 Optical coherence tomography. Science 254(5035):1178–81 [PubMed: 1957169]

Hunter JJ, Merigan WH, Schallek JB. 2019 Imaging retinal activity in the living eye. Annu. Rev. Vis. Sci 5:15–45 [PubMed: 31525142]

Izatt JA, Choma MA, Dhalla A-H. 2015 Theory of optical coherence tomography In Optical Coherence Tomography: Technology and Applications, ed. Drexler W, Fujimoto JG, pp. 65–94. Berlin: Springer. 2nd ed.

Jiang M, Esteve-Rudd J, Lopes VS, Diemer T, Lillo C, et al. 2015 Microtubule motors transport phagosomes in the RPE, and lack of KLC1 leads to AMD-like pathogenesis. J. Cell Biol 210(4):595–611 [PubMed: 26261180]

Jonnal RS, Besecker JR, Derby JC, Kocaoglu OP, Cense AJ, et al. 2010 Imaging outer segment renewal in living human cone photoreceptors. Opt. Express 18(5):5257–70 [PubMed: 20389538]

Jonnal RS, Gorczynska I, Migacz JV, Azimipour M, Zawadzki RJ, Werner JS. 2017 The properties of outer retinal band three investigated with adaptive-optics optical coherence tomography. Investig. Ophthalmol. Vis. Sci 58(11):4559–68 [PubMed: 28877320]

Jonnal RS, Kocaoglu OP, Wang Q, Lee S, Miller DT. 2012 Phase-sensitive imaging of the outer retina using optical coherence tomography and adaptive optics. Biomed. Opt. Express 3(1):104–24 [PubMed: 22254172]

Jonnal RS, Kocaoglu OP, Zawadzki RJ, Lee S-H, Werner JS, Miller DT. 2014 The cellular origins of the outer retinal bands in optical coherence tomography images. Investig. Ophthalmol. Vis. Sci 55(12):7904–18 [PubMed: 25324288]

Jonnal RS, Kocaoglu OP, Zawadzki RJ, Lee S-H, Werner JS, Miller DT. 2015 Author response: outer retinal bands. Investig. Ophthalmol. Vis. Sci 56(4):2507–10 [PubMed: 26066597]

Jonnal RS, Kocaoglu OP, Zawadzki RJ, Liu Z, Miller DT, Werner JS. 2016 A review of adaptive optics optical coherence tomography: technical advances, scientific applications, and the future. Investig. Ophthalmol. Vis. Sci 57(9):OCT51–68

Jonnal RS, Rha J, Zhang Y, Cense AJ, Gao W, Miller DT. 2007 In vivo functional imaging of human cone photoreceptors. Opt. Express 15(24):16141–60

Joo HR, Peterson BB, Haun TJ, Dacey DM. 2011 Characterization of a novel large-field cone bipolar cell type in the primate retina: evidence for selective cone connections. Vis. Neurosci 28(1):29–37 [PubMed: 21156090]

Ju MJ, Heisler M, Wahl D, Jian Y, Sarunic MV. 2017 Multiscale sensorless adaptive optics OCT angiography system for in vivo human retinal imaging. J. Biomed. Opt 22(12):1–10

Jung HW, Kurokawa K, Hinely JC, Crowell JA, Zhang F, et al. 2020 Method to evaluate spatial dynamics of inner retinal neurons near arcuate scotomas in glaucomatous patients. Proc. SPIE 11218:1121844

Jung HW, Liu J, Liu T, George A, Smelkinson MG, et al. 2019 Longitudinal adaptive optics fluorescence microscopy reveals cellular mosaicism in patients. JCI Insight. 4(6):124904 [PubMed: 30895942]

Kevany BM, Palczewski K. 2010 Phagocytosis ofretinal rod and cone photoreceptors. Physiology 25(1):8–15 [PubMed: 20134024]

Kocaoglu OP, Cense AJ, Jonnal RS, Wang Q, Lee S, et al. 2011a Imaging retinal nerve fiber bundles using optical coherence tomography with adaptive optics. Vision Res. 51(16):1835–44 [PubMed: 21722662]

Kocaoglu OP, Ferguson RD, Jonnal RS, Liu Z, Wang Q, et al. 2014a Adaptive optics optical coherence tomography with dynamic retinal tracking. Biomed. Opt. Express 5(7):2262–84 [PubMed: 25071963]

Kocaoglu OP, Lee S, Jonnal RS, Wang Q, Herde AE, et al. 2011b Imaging cone photoreceptors in three dimensions and in time using ultrahigh resolution optical coherence tomography with adaptive optics. Biomed. Opt. Express 2(4):748–63 [PubMed: 21483600]

Kocaoglu OP, Liu Z, Zhang F, Kurokawa K, Jonnal RS, Miller DT. 2016 Photoreceptor disc shedding in the living human eye. Biomed. Opt. Express 7(11):4554–68 [PubMed: 27895995]

Kocaoglu OP, Turner TL, Liu Z, Miller DT. 2014b Adaptive optics optical coherence tomography at 1 MHz. Biomed. Opt. Express 5(12):4186–200 [PubMed: 25574431]

Kolb H, Linberg KA, Fisher SK. 1992 Neurons of the human retina: a Golgi study. J. Comp. Neurol 318(2):147–87 [PubMed: 1374766]

Kurokawa K, Crowell JA, Zhang F, Lassoued A, Miller DT. 2019 Measuring neuron loss in the retinal ganglion cell layer in healthy subjects. Investig. Ophthalmol. Vis. Sci 60(9):1781

Kurokawa K, Crowell JA, Zhang F, Miller DT. 2020 Suite of methods for assessing inner retinal temporal dynamics across spatial and temporal scales in the living human eye. Neurophotonics 7(1):015013 [PubMed: 32206680]

Kurokawa K, Liu Z, Miller DT. 2017 Adaptive optics optical coherence tomography angiography for morphometric analysis of choriocapillaris [invited]. Biomed. Opt. Express 8(3):1803–22 [PubMed: 28663867]

Kurokawa K, Sasaki K, Makita S, Hong Y-J, Yasuno Y. 2012 Three-dimensional retinal and choroidal capillary imaging by power Doppler optical coherence angiography with adaptive optics. Opt. Express 20(20):22796–812 [PubMed: 23037430]

Laforest T, Künzi M, Kowalczuk L, Carpentras D, Behar-Cohen F, Moser C. 2020 Transscleral optical phase imaging of the human retina. Nat. Photon 14(7):439–45

LaRocca F, Nankivil D, DuBose T, Toth CA, Farsiu S, Izatt JA. 2016 In vivo cellular-resolution retinal imaging in infants and children using an ultracompact handheld probe. Nat. Photon 10(9):2–11

Lassoued A, Zhang F, Kurokawa K, Liu Y, Crowell JA, Miller DT. 2020 Measuring dysfunction of cone photoreceptors in retinitis pigmentosa with phase-sensitive AO-OCT. Ophthalmic Technol. XXX:1121815

Lazarus HS, Hageman GS. 1994 In situ characterization of the human hyalocyte. Arch. Ophthalmol 112(10):1356–62 [PubMed: 7945040]

Lee S-H, Werner JS, Zawadzki RJ. 2013 Improved visualization of outer retinal morphology with aberration cancelling reflective optical design for adaptive optics-optical coherence tomography. Biomed. Opt. Express 4(11):2508–17 [PubMed: 24298411]

Lei Y, Garrahan N, Hermann B, Fautsch MP, Johnson DH, et al. 2011 Transretinal degeneration in ageing human retina: a multiphoton microscopy analysis. Br. J. Ophthalmol 95(5):727–30 [PubMed: 21183516]

Liang J, Williams DR, Miller DT. 1997 Supernormal vision and high-resolution retinal imaging through adaptive optics. J. Opt. Soc. Am. A 14(11):2884–92

Litts K, Zhang Y, Freund K, Curcio C. 2018 Optical coherence tomography and histology of age-related macular degeneration support mitochondria as reflectivity sources. Retina 38(3):445–61 [PubMed: 29210936]

Liu Z, Hammer DX, Saeedi O. 2019a Multimodal adaptive optics imaging of ganglion cells in patients with primary open angle glaucoma. Investig. Ophthalmol. Vis. Sci 60(9):4608

Liu Z, Kocaoglu OP, Miller DT. 2016 3D imaging of retinal pigment epithelial cells in the living human retina. Investig. Ophthalmol. Vis. Sci 57(9):OCT533–43 [PubMed: 26873512]

Liu Z, Kocaoglu OP, Turner TL, Miller DT. 2015 Modal content of living human cone photoreceptors. Biomed. Opt. Express 6(9):3378–404 [PubMed: 26417509]

Liu Z, Kurokawa K, Hammer DX, Miller DT. 2019b In vivo measurement of organelle motility in human retinal pigment epithelial cells. Biomed. Opt. Express 10(8):4142–58 [PubMed: 31453000]

Liu Z, Kurokawa K, Zhang F, Lee JJ, Miller DT. 2017 Imaging and quantifying ganglion cells and other transparent neurons in the living human retina. PNAS 114(48):12803–8 [PubMed: 29138314]

Liu Z, Tam J, Saeedi O, Hammer DX. 2018 Trans-retinal cellular imaging with multimodal adaptive optics. Biomed. Opt. Express 9(9):4246–62 [PubMed: 30615699]

Martinez-Conde S, Macknik SL, Hubel DH. 2004 The role of fixational eye movements in visual perception. Nat. Rev. Neurosci 5(3):229–40 [PubMed: 14976522]

Medeiros FA, Zangwill LM, Anderson DR, Liebmann JM, Girkin CA, et al. 2012 Estimating the rate of retinal ganglion cell loss in glaucoma. Am. J. Ophthalmol 154(5):814–24.e1 [PubMed: 22840484]

Merino D, Loza-Alvarez P 2016 Adaptive optics scanning laser ophthalmoscope imaging: technology update. Clin. Ophthalmol 10:743–55 [PubMed: 27175057]

Migacz JV, Gorczynska I, Azimipour M, Jonnal RS, Zawadzki RJ, Werner JS. 2019 Megahertz-rate optical coherence tomography angiography improves the contrast of the choriocapillaris and choroid in human retinal imaging. Biomed. Opt. Express 10(1):50–65 [PubMed: 30775082]

Miller DT, Qu J, Jonnal RS, Thorn KE. 2003 Coherence gating and adaptive optics in the eye Proceedings of Coherence Domain Optical Methods and Optical Coherence Tomography in Biomedicine VII, pp. 65–72. Bellingham, WA: SPIE

Miller DT, Williams DR, Morris GM, Liang J. 1996 Images of cone photoreceptors in the living human eye. Vision Res. 36(8):1067–79 [PubMed: 8762712]

Morgan JIW 2016 The fundus photo has met its match: optical coherence tomography and adaptive optics ophthalmoscopy are here to stay. Ophthalmic Physiol. Opt 36(3):218–39 [PubMed: 27112222]

Mourant JR, Freyer JP, Hielscher AH, Eick AA, Shen D, Johnson TM. 1998 Mechanisms of light scattering from biological cells relevant to noninvasive optical-tissue diagnostics. Appl. Opt 37(16):3586–93 [PubMed: 18273328]

Ogden TE. 1984 Nerve fiber layer of the primate retina: morphometric analysis. Investig. Ophthalmol. Vis. Sci 25(1):19–29 [PubMed: 6698729]

Paques M, Meimon S, Rossant F, Rosenbaum D, Mrejen S, et al. 2018 Adaptive optics ophthalmoscopy: application to age-related macular degeneration and vascular diseases. Prog. Retin. Eye Res 66:1–16 [PubMed: 30010022]

Pascolini D, Mariotti SP 2012 Global estimates of visual impairment: 2010. Br. J. Ophthalmol 95:614–18

Pfäffle C, Spahr H, Kutzner L, Burhan S, Hilge F, et al. 2019 Simultaneous functional imaging of neuronal and photoreceptor layers in living human retina. Opt. Lett 44(23):5671–74 [PubMed: 31774751]

Pircher M, Kroisamer JS, Felberer F, Sattmann H, Götzinger E, Hitzenberger CK. 2011 Temporal changes of human cone photoreceptors observed in vivo with SLO/OCT. Biomed. Opt. Express 2(1):100–12

Pircher M, Zawadzki RJ. 2017 Review of adaptive optics OCT (AO-OCT): principles and applications for retinal imaging [invited]. Biomed. Opt. Express 8(5):2536–62 [PubMed: 28663890]

Pollreisz A, Messinger JD, Sloan KR, Mittermueller TJ, Weinhandl AS, et al. 2018 Visualizing melanosomes, lipofuscin, and melanolipofuscin in human retinal pigment epithelium using serial block face scanning electron microscopy. Exp. Eye Res 166:131–39 [PubMed: 29066281]

Porter J, Queener HM, Lin J, Thorn KE, Awwal A, eds. 2006 Adaptive Optics for Vision Science: Principles, Practices, Design and Applications. New York: Wiley

Potsaid B, Gorczynska I, Srinivasan VJ, Chen Y, Jiang J, et al. 2008 Ultrahigh speed spectral/Fourier domain OCT ophthalmic imaging at 70,000 to 312,500 axial scans per second. Opt. Express 16(19):15149–69 [PubMed: 18795054]

Quigley HA. 1999 Neuronal death in glaucoma. Prog. Retin. Eye Res 18(1):39–57 [PubMed: 9920498]

Quigley HA. 2011 Glaucoma. Lancet 377(9774):1367–77 [PubMed: 21453963]

Rodieck RW. 1998 The First Steps in Seeing. Sunderland, MA: Sinauer Assoc.

Roorda AJ, Duncan JL. 2015 Adaptive optics ophthalmoscopy. Annu. Rev. Vis. Sci 1:19–50 [PubMed: 26973867]

Roorda AJ, Williams DR. 1999 The arrangement of the three cone classes in the living human eye. Nature 397(6719):520–22 [PubMed: 10028967]

Ruggiero L, Finnemann SC. 2014 Rhythmicity of the retinal pigment epithelium In The Retina and Circadian Rhythms, ed. Tosini G, Iuvone PM, McMahon DG, Collin SP, pp. 95–112. Berlin: Springer

Sabesan R, Hofer H, Roorda AJ. 2015 Characterizing the human cone photoreceptor mosaic via dynamic photopigment densitometry. PLOS ONE 10(12):e0144891 [PubMed: 26660894]

Salas M, Augustin M, Ginner L, Kumar A, Baumann B, et al. 2017 Visualization of micro-capillaries using optical coherence tomography angiography with and without adaptive optics. Biomed. Opt. Express 8(1):207–22 [PubMed: 28101412]

Schnapf JL, Nunn BJ, Meister M, Baylor DA. 1990 Visual transduction in cones of the monkey Macaca fascicularis. J. Physiol 427:681–713 [PubMed: 2100987]

Scoles D, Sulai YN, Langlo CS, Fishman GA, Curcio CA, et al. 2014 In vivo imaging of human cone photoreceptor inner segments. Investig. Ophthalmol. Vis. Sci 55(7):4244–51 [PubMed: 24906859]

South FA, Kurokawa K, Liu Z, Liu Y-Z, Miller DT, Boppart SA. 2018 Combined hardware and computational optical wavefront correction. Biomed. Opt. Express 9(6):2562–74 [PubMed: 30258673]

Spaide RF, Curcio CA. 2011 Anatomical correlates to the bands seen in the outer retina by optical coherence tomography: literature review and model. Retina 31(8):1609–19 [PubMed: 21844839]

Staurenghi G, Sadda S, Chakravarthy U, Spaide RF, Int. Nomencl. Opt. Coherence Tomogr. (IN* OCT) Panel. 2014 Proposed lexicon for anatomic landmarks in normal posterior segment spectral-domain optical coherence tomography: the IN* OCT consensus. Ophthalmology 121(8):1572–78 [PubMed: 24755005]

Steinberg RH, Wood I, Hogan MJ. 1977 Pigment epithelial ensheathment and phagocytosis of extrafoveal cones in human retina. Philos. Trans. R. Soc. Lond. Ser. B 277(958):459–71 [PubMed: 16301]

Stockman A, Sharpe LT. 2000 The spectral sensitivities of the middle- and long-wavelength-sensitive cones derived from measurements in observers of known genotype. Vis. Res 40(13):1711–37 [PubMed: 10814758]

Tanna H, Dubis AM, Ayub N, Tait DM, Rha J, et al. 2010 Retinal imaging using commercial broadband optical coherence tomography. Br. J. Ophthalmol 94(3):372–76 [PubMed: 19770161]

Torti C, Povazay B, Hofer B, Unterhuber A, Carroll J, et al. 2009 Adaptive optics optical coherence tomography at 120,000 depth scans/s for non-invasive cellular phenotyping of the living human retina. Opt. Express 17(22):19382–400 [PubMed: 19997159]

Vagaja NN, Chinnery HR, Binz N, Kezic JM, Rakoczy EP, McMenamin PG. 2012 Changes in murine hyalocytes are valuable early indicators of ocular disease. Investig. Ophthalmol. Vis. Sci 53(3):1445–51 [PubMed: 22297487]

Volpe NJ, Simonett J, Fawzi AA, Siddique T. 2015 Ophthalmic manifestations of amyotrophic lateral sclerosis (an American Ophthalmological Society Thesis). Trans. Am. Ophthalmol. Soc 113:T12 [PubMed: 26877563]

Wang L, Dong J, Cull G, Fortune B, Cioffi GA. 2003 Varicosities of intraretinal ganglion cell axons in human and nonhuman primates. Investig. Ophthalmol. Vis. Sci 44(1):2–9 [PubMed: 12506048]

Watanabe M, Rodieck RW. 1989 Parasol and midget ganglion cells of the primate retina. J. Comp. Neurol 289(3):434–54 [PubMed: 2808778]

Weinreb RN, Aung T, Medeiros FA. 2014 The pathophysiology and treatment of glaucoma: a review. JAMA 311(18):1901–11 [PubMed: 24825645]

Weiter JJ, Delori FC, Wing GL, Fitch KA. 1986 Retinal pigment epithelial lipofuscin and melanin and choroidal melanin in human eyes. Investig. Ophthalmol. Vis. Sci 27(2):145–52 [PubMed: 3943941]

Wells-Gray EM, Choi SS, Ohr M, Cebulla CM, Doble N. 2019 Photoreceptor identification and quantitative analysis for the detection of retinal disease in AO-OCT imaging. Ophthalmic Technol. XXIX:108580O-1–9

Wells-Gray EM, Choi SS, Slabaugh M, Weber P, Doble N. 2018a Inner retinal changes in primary open-angle glaucoma revealed through adaptive optics-optical coherence tomography. J. Glaucoma 27(11):1025–28 [PubMed: 30095607]

Wells-Gray EM, Choi SS, Zawadzki RJ, Finn SC, Greiner C, et al. 2018b Volumetric imaging of rod and cone photoreceptor structure with a combined adaptive optics-optical coherence tomography-scanning laser ophthalmoscope. J. Biomed. Opt 23(3):1–15

Werner JS, Keltner JL, Zawadzki RJ, Choi SS. 2011 Outer retinal abnormalities associated with inner retinal pathology in nonglaucomatous and glaucomatous optic neuropathies. Eye 25(3):279–89 [PubMed: 21293495]

Wilk MA, Huckenpahler AL, Collery RF, Link BA, Carroll J. 2017 The effect of retinal melanin on optical coherence tomography images. Transl. Vis. Sci. Technol 6(2):8

Wilson JD, Cottrell WJ, Foster TH. 2007 Index-of-refraction-dependent subcellular light scattering observed with organelle-specific dyes. J. Biomed. Opt 12(1):014010 [PubMed: 17343485]

Wilson JD, Foster TH. 2007 Characterization of lysosomal contribution to whole-cell light scattering by organelle ablation. J. Biomed. Opt 12(3):030503 [PubMed: 17614706]

Wong KSK, Jian Y, Cua M, Bonora S, Zawadzki RJ, Sarunic MV. 2015 In vivo imaging of human photoreceptor mosaic with wavefront sensorless adaptive optics optical coherence tomography. Biomed. Opt. Express 6(2):580–90 [PubMed: 25780747]

Young RW. 1967 The renewal of photoreceptor cell outer segments. J. Cell Biol 33(1):61–72 [PubMed: 6033942]

Young RW, Bok D. 1969 Participation of the retinal pigment epithelium in the rod outer segment renewal process. J. Cell Biol 42(2):392–403 [PubMed: 5792328]

Zawadzki RJ, Cense AJ, Zhang Y, Choi SS, Miller DT, Werner JS. 2008 Ultrahigh-resolution optical coherence tomography with monochromatic and chromatic aberration correction. Opt. Express 16(11):8126–43 [PubMed: 18545525]

Zawadzki RJ, Choi SS, Jones SM, Oliver SS, Werner JS. 2007 Adaptive optics-optical coherence tomography: optimizing visualization of microscopic retinal structures in three dimensions. J. Opt. Soc. Am. A 24(5):1373–83

Zawadzki RJ, Jones SM, Olivier SS, Zhao M, Bower BA, et al. 2005 Adaptive-optics optical coherence tomography for high-resolution and high-speed 3D retinal in vivo imaging. Opt. Express 13(21):8532–46 [PubMed: 19096728]

Zhang F 2019 Imaging physiological activities of photoreceptors with adaptive optics optical coherence tomography in the living human eye. PhD thesis, Indiana Univ, Indianapolis

Zhang F, Kurokawa K, Lassoued A, Crowell JA, Miller DT. 2019 Cone photoreceptor classification in the living human eye from photostimulation-induced phase dynamics. PNAS 116:7951–56 [PubMed: 30944223]

Zhang F, Liu Z, Kurokawa K, Miller DT. 2017 Tracking dynamics of photoreceptor disc shedding with adaptive optics-optical coherence tomography. Ophthalmic Technol. XXVII:1004517

Zhang P, Zawadzki RJ, Goswami M, Nguyen PT, Yarov-Yarovoy V, et al. 2017In vivo optophysiology reveals that G-protein activation triggers osmotic swelling and increased light scattering of rod photoreceptors. PNAS 114(14):E2937–46 [PubMed: 28320964]

Zhang Q-X, Lu R-W, Messinger JD, Curcio CA, Guarcello V, Yao X-C. 2013 In vivo optical coherence tomography of light-driven melanosome translocation in retinal pigment epithelium. Sci. Rep 3(1):2644 [PubMed: 24025778]

Zhang T, Kho AM, Srinivasan VJ. 2019 Improving visible light OCT of the human retina with rapid spectral shaping and axial tracking. Biomed. Opt. Express 10(6):2918–31 [PubMed: 31259062]

Zhang Y, Cense AJ, Rha J, Jonnal RS, Gao W, et al. 2006 High-speed volumetric imaging of cone photoreceptors with adaptive optics spectral-domain optical coherence tomography. Opt. Express 14(10):4380–94 [PubMed: 19096730]

Zhang Y, Rha J, Jonnal RS, Miller DT. 2005 Adaptive optics parallel spectral domain optical coherence tomography for imaging the living retina. Opt. Express 13(12):4792–811 [PubMed: 19495398]

Author Manuscript

Author Manuscript

Author Manuscript

Author Manuscript

DESCRIPTION OF OPTICAL COHERENCE TOMOGRAPHY

OCT is the optical analogy of ultrasonography, measuring the time of flight of light, rather than sound, to generate cross-sectional and volume images of a sample (e.g., the retina). However, light travels many orders of magnitude faster than sound, and therefore differences in its time of flight inside the sample are too short to be resolved directly with electronic detectors. OCT solves this problem using a technique called low-coherence interferometry.

Using interferometry, light backscattered from the sample placed in one arm of the interferometer is interfered with light reflected from a planar mirror placed in the other (reference) arm. Coherent interference occurs if the path lengths of the two arms match to within the coherence length of the interferometer's light source, i.e., they have the same time of flight. OCT uses a broadband light source to detect the interference at each wavelength (spectral interferogram). This interference is used to measure the backscatter's depth location in the sample, strength (reflectance), and phase (modulo-2π optical path length difference between the backscatter's location in the sample arm and the planar mirror location in the reference arm). Thus, OCT's axial resolution is set by the light source's coherence length (typically 3 to 10 microns in tissue for most OCT systems) and independent of the system's numeric aperture, which determines axial resolution in conventional optical systems. Furthermore, the ability to detect phase (called phase-sensitive detection) enables subwavelength optical path length changes, which are orders of magnitude smaller than OCT's axial resolution, to be detected in the tissue sample.

OPTICAL COHERENCE TOMOGRAPHY IMAGE TERMINOLOGY

OCT volume images are described using terminology borrowed from ultrasonography: A-scan, B-scan, and C-scan. An A-scan is a single column of pixels that extends over the full depth (Z) of the volume image and traverses all the layers of the retina. An OCT volume is composed of many A-scans that are arranged in a 2D rectilinear array. A B-scan is composed of a contiguous line of A-scans, thus forming a 2D cross-sectional (XZ) slice through the volume image. B-scan images are useful for displaying the laminar profile of the retinal layers. A C-scan slices perpendicularly through all A-scans, thus forming a 2D en face (XY) slice at one depth (Z) in the volume. C-scan images are useful for displaying cells in one retinal layer.

OPTICAL COHERENCE TOMOGRAPHY IMAGING APPROACHES

There are three broad categories of OCT systems: TD-OCT, SD-OCT, and SS-OCT. TD-OCT was introduced by Huang et al. (1991) almost three decades ago and spatially resolves backscatter across depth in the retina by rapidly changing the optical path length of the reference arm in a scanning manner. In the early to mid-2000s, SD-OCT and SS-OCT were introduced and largely replaced TD-OCT because of their higher efficiency and imaging speed. SD-OCT simultaneously captures all sample reflections at a given entry point with a high-speed spectrometer, thereby directly recording the interference at each wavelength. SS-OCT follows a similar strategy, but implements it differently by using a specialized light source that rapidly sweeps across the wavelengths of its spectrum coupled with a point detector that synchronizes capture of interference at each wavelength. TD-OCT, SD-OCT, and SS-OCT are further divided by how they illuminate the retina: point-scanning, line field, and full field. Extensive theoretical and quantitative descriptions of these various methods are available in the literature for the interested reader (Drexler & Fujimoto 2015).

MEASURING CHANGES IN THE CONE OUTER SEGMENT LENGTH

The bright punctate reflection of each cone cell that is visible in en face is a superposition of two dominant reflections, one at each end of the cone outer segment: IS/OS and COST (see Figures 4 and 7a,c). Thus the axial separation between IS/OS and COST reflections is considered a measure of the cone outer segment length. The 3D resolution of AO-OCT is sufficient to resolve these reflections in three dimensions and enables changes in outer segment length to be measured and tracked with considerable precision. AO-OCT's sensitivity to axial displacements (or, more precisely, OPL) inside single cone cells ranges from approximately 400 nm (>10 times better than its axial resolution) when using the cone reflection's amplitude (Kocaoglu et al. 2016, F. Zhang et al. 2017) to a mere 5 nm (one-fifth the spacing of outer segment discs) when using the cone reflection's phase as measured with phase-sensitive AO-OCT (F. Zhang et al. 2017).

SUMMARY POINTS

1. Visualizing single retinal cells and their processes in the living human eye is largely dictated by requirements in spatial resolution, sensitivity, and temporal bandwidth of the imaging system.

2. Today's AO-OCT is much better matched to these requirements than it was just a few years ago, now providing pristine 3D views of the cellular retina.

3. AO-OCT allows visualization of cells and cell components, most of which are highly transparent, across the entire retinal thickness. This includes RPE cells, cone and rod photoreceptors, bipolar cells, amacrine cells, retinal ganglion cells, and macrophage-like cells; cell somas are observed in both nuclear layers and the GCL.

4. Cone photoreceptors extend over a significant portion of the retinal thickness, yet much of their structure has not been imaged due to their high transparency. AO-OCT permits a much better appreciation of the cone's full extent.

5. AO-OCT allows visualizing and quantifying physiological processes in retinal cells that occur over a wide range of temporal scales, from milliseconds to years. Processes have been measured across the entire retinal thickness.

6. Phase-sensitive AO-OCT enables detection of extremely minute (5 nm) axial changes in tissue. Physiological processes that induce optical changes on the scale of molecules have been measured.

7. Attribution of image features to the underlying anatomy is essential for AO-OCT's scientific and clinical use but remains challenging.

FUTURE ISSUES

1. OCT remains a rapidly advancing technology. We expect dramatic improvements in how AO-OCT is applied to the eye and the types of structures and processes that we can see with it.

2. All major neurons in the retina should be identifiable with AO-OCT in the next few years. Less certainty holds for the supporting neuroglial cells that remain largely elusive to our imaging.

3. Most physiological processes in the retina induce extremely small optical changes. Improved methods to stabilize and extract these changes in the AO-OCT image are imperative for better detection of these processes.
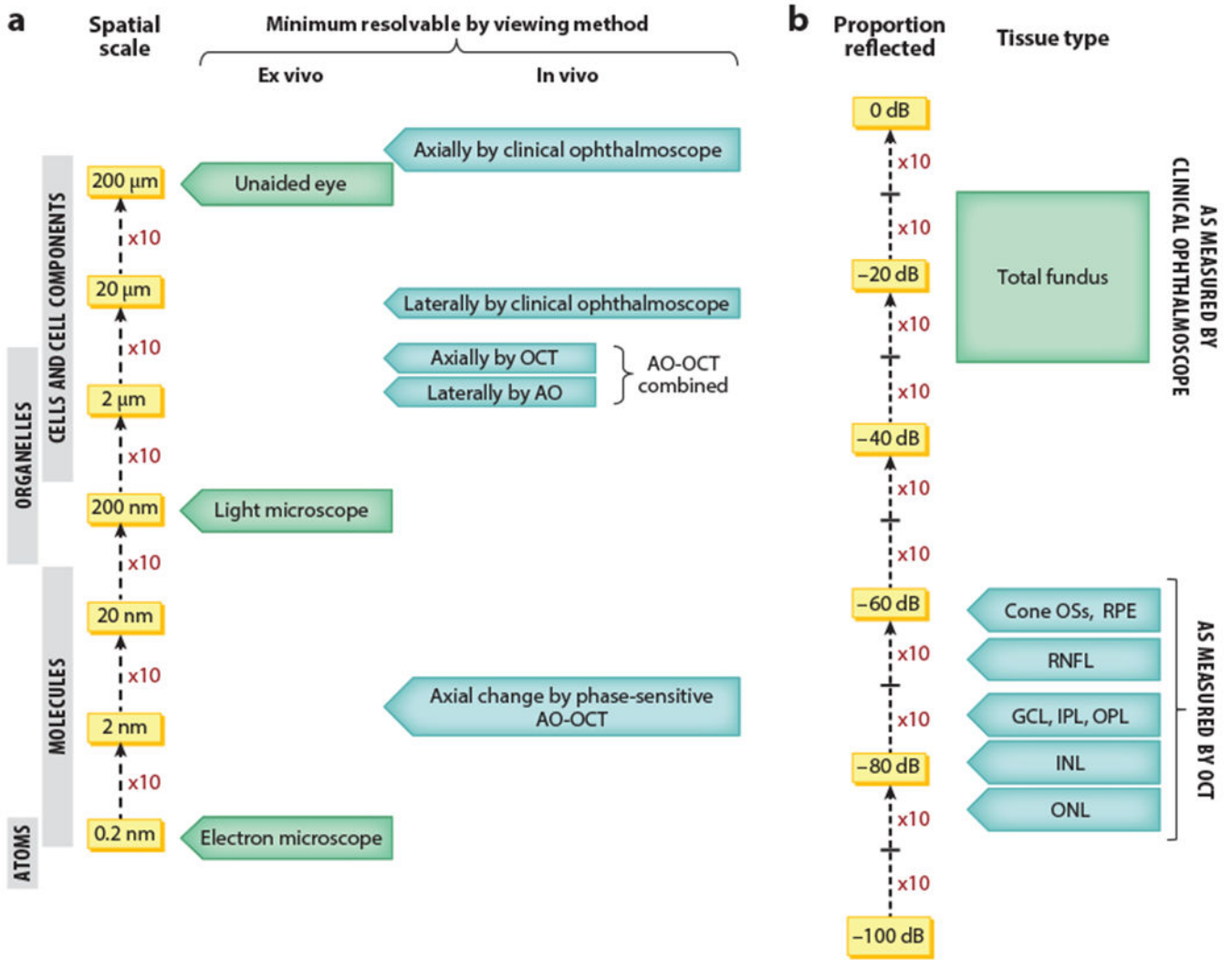
Figure 1.

Our view of the microscopic retina depends on the physical size and optical properties of the tissue and the type of viewing method used. (*a*) Spatial scale shows the sizes of human retinal cells (e.g., photoreceptor and Müller cells) and cell components (e.g., soma, dendrites, and axons) and their subcomponent parts (organelles, molecules, and atoms). For simplicity, spatial scale encompasses both lateral and axial dimensions. Labeled are the units in which the cell components and subcomponents are resolved in different types of ex vivo (histological) and in vivo (through the eye's optics) viewing. The clinical ophthalmoscope corresponds to a flood-illuminated fundus camera. (*b*) Reflectance scale shows the proportion of light entering the eye that is reflected and exits the eye. As measured by a clinical ophthalmoscope, total reflectance of the fundus (retina, choroid, and sclera combined) varies by two orders of magnitude (−10 to −30 dB) depending on the wavelength of light used (400 to 1,000 nm) (Delori & Pflibsen 1989). As measured by clinical OCT, the reflectance is spatially resolved in depth and limited largely to singly scattered light, making each resolved reflection much weaker than the clinical ophthalmoscope total reflectance. OCT reflections vary by approximately 2.5 orders of magnitude (−60 to −85 dB) depending

on tissue type and retinal layer. This range is derived from the normalized retinal reflectance profile in clinical OCT images (e.g., Chen et al. 2013) and the typical OCT system sensitivity (−95 dB) and dynamic range in retinal tissue (35 dB). Abbreviations: AO, adaptive optics; GCL, ganglion cell layer; INL, inner nuclear layer; IPL, inner plexiform layer; OCT, optical coherence tomography; ONL, outer nuclear layer; OPL, outer plexiform layer; OS, outer segment; RNFL, retinal nerve fiber layer; RPE, retinal pigment epithelium.
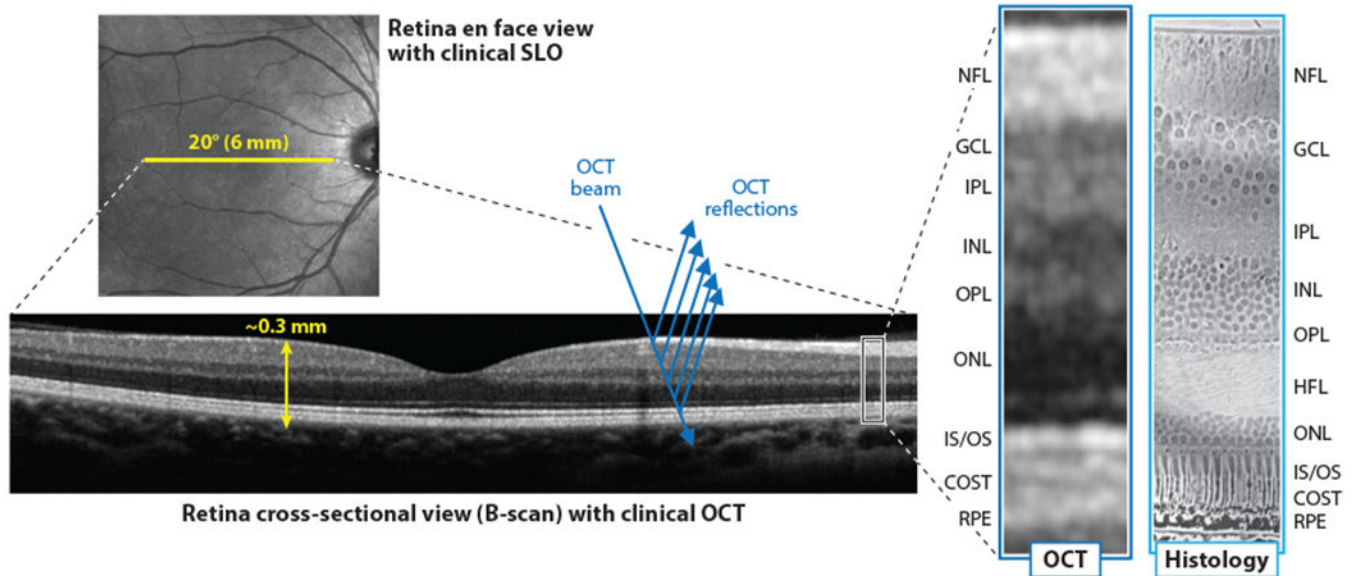
Figure 2.
Clinical OCT's pristine view of the retina is lost at the cellular scale. (*Left*) OCT cross-section (Spectralis, Heidelberg Engineering) bisects the fovea along the horizontal meridian and reveals banding of the principal neural layers. (*Right*) To assess cellular content, a magnified section of the OCT image is scaled to a comparable histologic cross-section of the human retina. Note that the mottled appearance of the OCT image is primarily speckle noise. The histologic cross-section is adapted with permission from Boycott et al. (1969). Abbreviations: COST, cone outer segment tip; GCL, ganglion cell layer; HFL, Henle's fiber layer; INL, inner nuclear layer; IPL, inner plexiform layer; IS/OS, inner segment/outer segment junction; NFL, nerve fiber layer; OCT, optical coherence tomography; ONL, outer nuclear layer; OPL, outer plexiform layer; RPE, retinal pigment epithelium; SLO, scanning laser ophthalmoscopy.
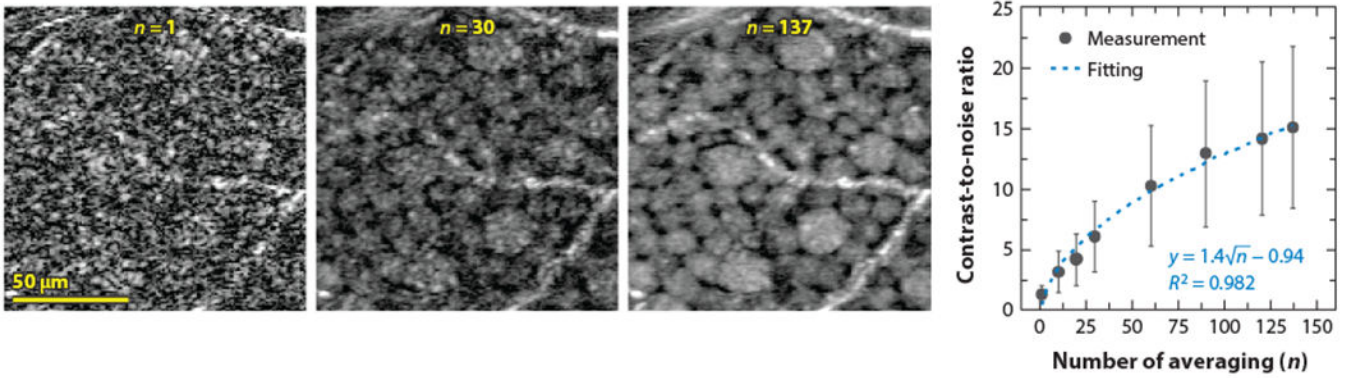
Figure 3.

Averaging registered AO-OCT images improves clarity of GCL somas. Magnified view of the same small patch of retina is shown with different amounts of averaging ($n = 1$, 30, and 137 images). Images are from 12° to 13.5° temporal to the fovea in the same subject. The plot shows the CNR of individual GCL somas computed as a function of number of images averaged. CNR was defined as the difference between the soma maximum and minimum amplitudes (after averaging all soma images, approximately 140) divided by the standard deviation of the soma noise (after subtracting the contribution of the soma structure). Error bars denote ±1 SD. CNR increase follows the square root of the number of images (*dashed curve*). Figure adapted from Liu et al. (2017). Abbreviations: AO-OCT, adaptive optics optical coherence tomography; CNR, contrast-to-noise ratio; GCL, ganglion cell layer; SD, standard deviation.
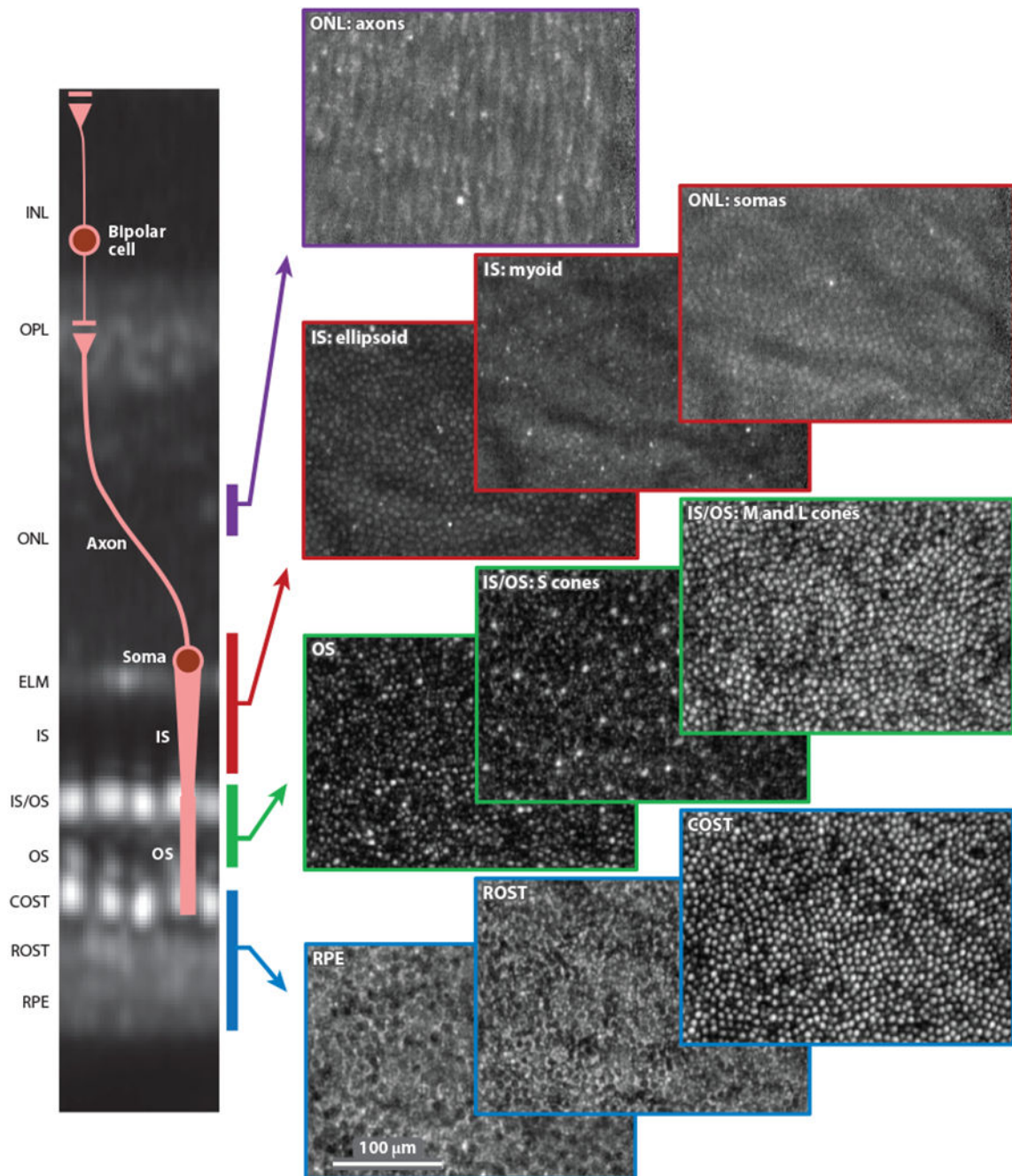
Figure 4.
AO-OCT volume image of the outer retina of a 52-year-old normal subject. Ten en face (C-scan) images are shown selected from the volume and color-coded by depth in the outer retina, as denoted in the cross-sectional slice (B-scan) on the left. Each C-scan image is normalized to itself and presented on a log intensity scale. The AO-OCT volume image is an average of approximately 2,200 registered volumes that were acquired at 3.7° temporal to the fovea. In flythrough Supplemental Video 1 of the volume, en face frames are spaced 2 μm in depth. Video adapted from F. Zhang et al. (2019). Abbreviations: AO-OCT, adaptive

optics optical coherence tomography; COST, cone outer segment tip; ELM, external limiting membrane; INL, inner nuclear layer; IS, inner segment; IS/OS, inner segment/outer segment junction; ONL, outer nuclear layer; OPL, outer plexiform layer; OS, outer segment; ROST, rod outer segment tip; RPE, retinal pigment epithelium.
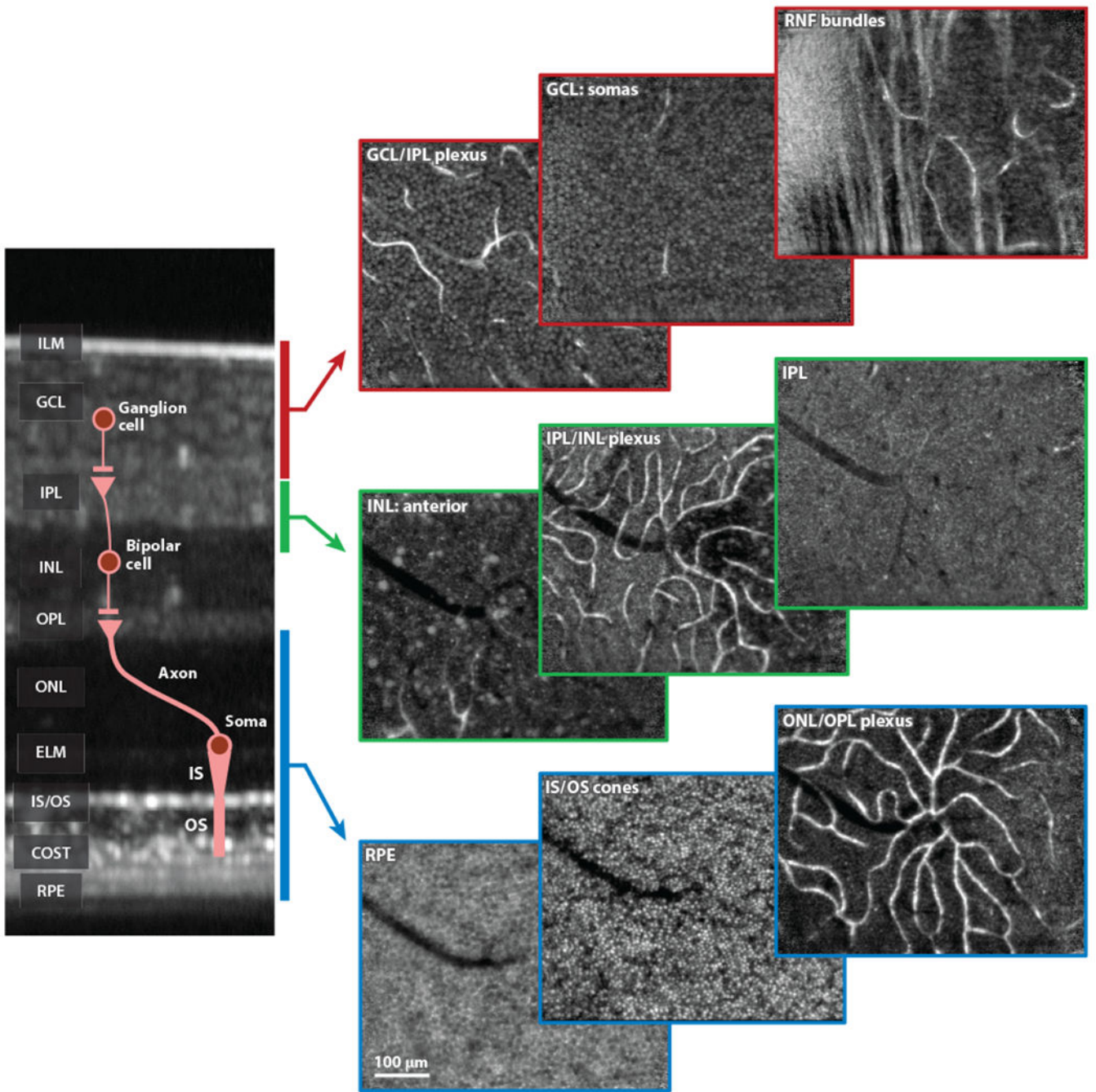
Figure 5.

Through-focus AO-OCT volume image preserves image sharpness over full retinal thickness and reveals cellular details at all depths. Nine en face (C-scan) images are shown selected from the volume and color-coded by depth in the retina, as denoted in the cross-sectional slice (B-scan) on the left. Each en face image is normalized to itself and presented on a nonlinear intensity scale with high dynamic range compression. The AO-OCT volume image is a composite of approximately 1,300 registered volumes of different focus that were acquired at 3.75° temporal to the fovea of a 26-year-old normal subject. In flythrough

Supplemental Video 2 of the volume, en face frames are spaced 1 μm in depth. Video adapted from K. Kurokawa, N. Do, J.A. Crowell, J.J. Lee & D.T. Miller (unpublished manuscript). Abbreviations: AO-OCT, adaptive optics optical coherence tomography; COST, cone outer segment tip; ELM, external limiting membrane; GCL, ganglion cell layer; ILM, inner limiting membrane; INL, inner nuclear layer; IPL, inner plexiform layer; IS, inner segment; IS/OS, inner segment/outer segment junction; ONL, outer nuclear layer; OPL, outer plexiform layer; OS, outer segment; RNF, retinal nerve fiber; ROST, rod outer segment tip; RPE, retinal pigment epithelium.
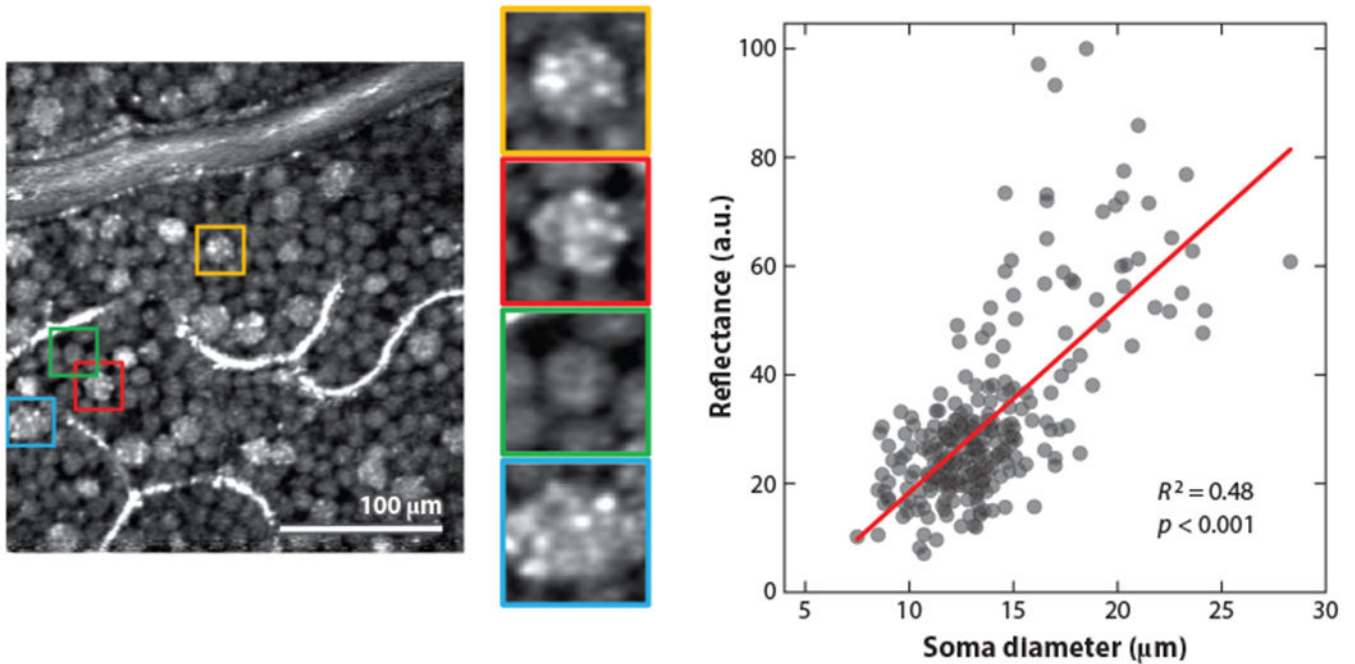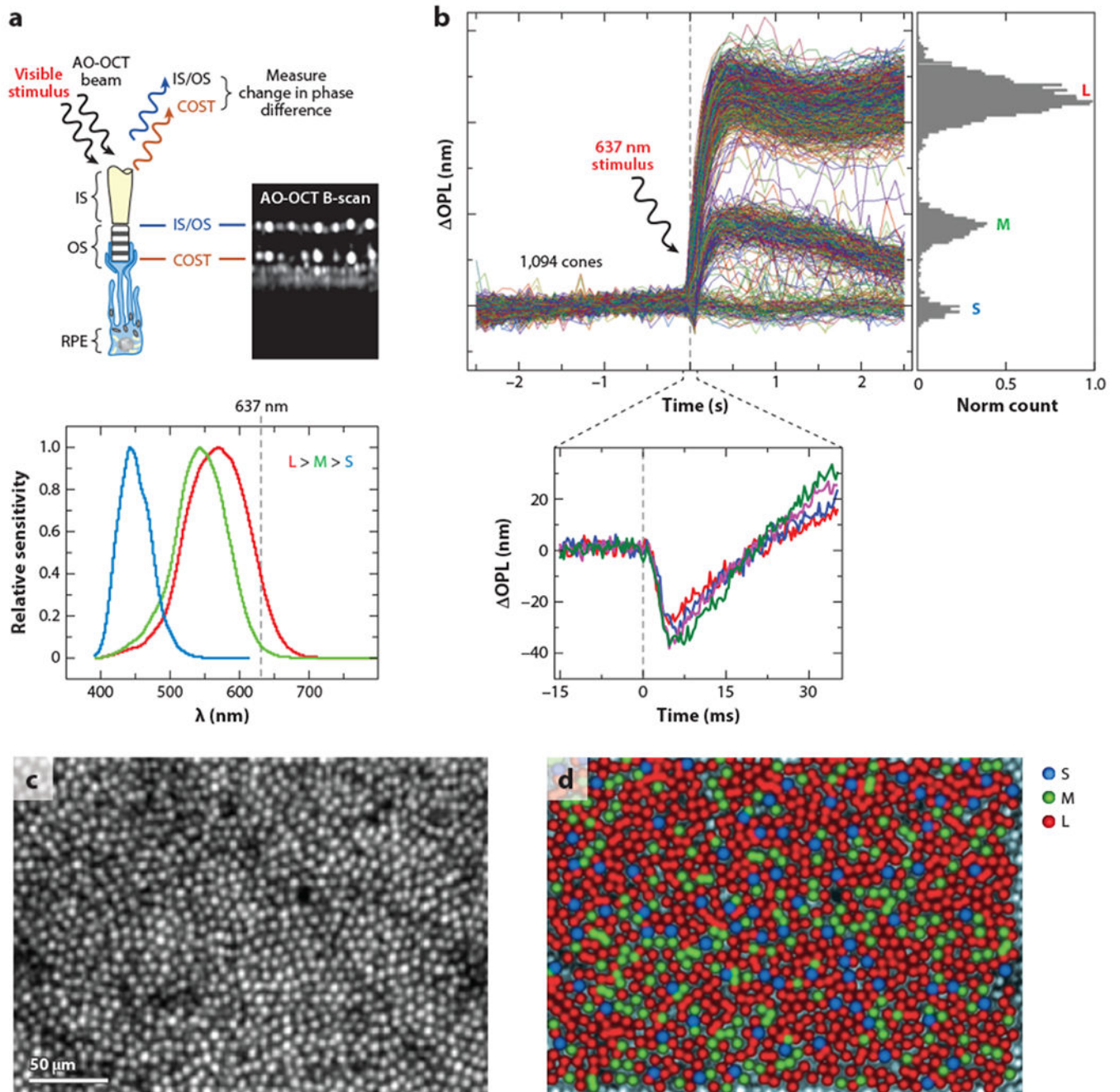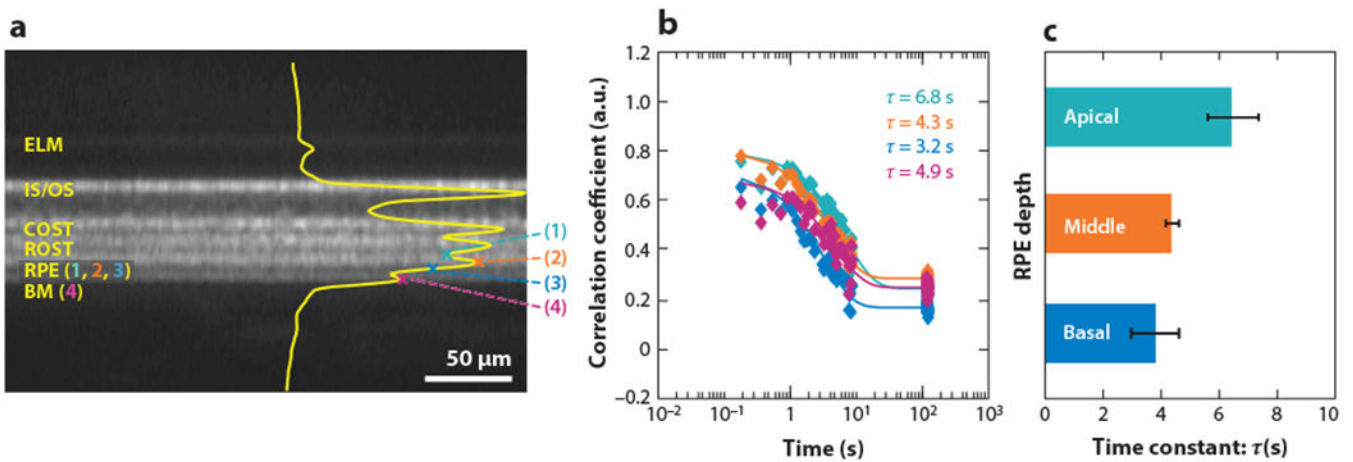
Figure 6.
Ganglion cell layer (GCL) somas have unique reflectance properties, as illustrated by this representative example at 12–13.5° temporal to the fovea. (*Left*) En face image of GCL extracted from a 562-volume average reveals a mosaic of somas whose reflectance varies between and within cells. All somas are at the same retinal depth. Some somas present a characteristic pattern of punctate reflections; three exemplary examples are shown in the colored insets (*orange*, *red*, and *aqua blue*). The green colored inset shows a soma without punctate reflections. (*Right*) Representative mean reflectance (amplitude/pixel measured at soma center) of 268 GCL somas is plotted against soma diameter. The 268 GCL somas were those identified in the en face image. The red line shows the linear regression curve and indicates that larger somas are generally more reflective than the smaller ones ($p < 0.001$). The subcellular source of this variation is unknown.
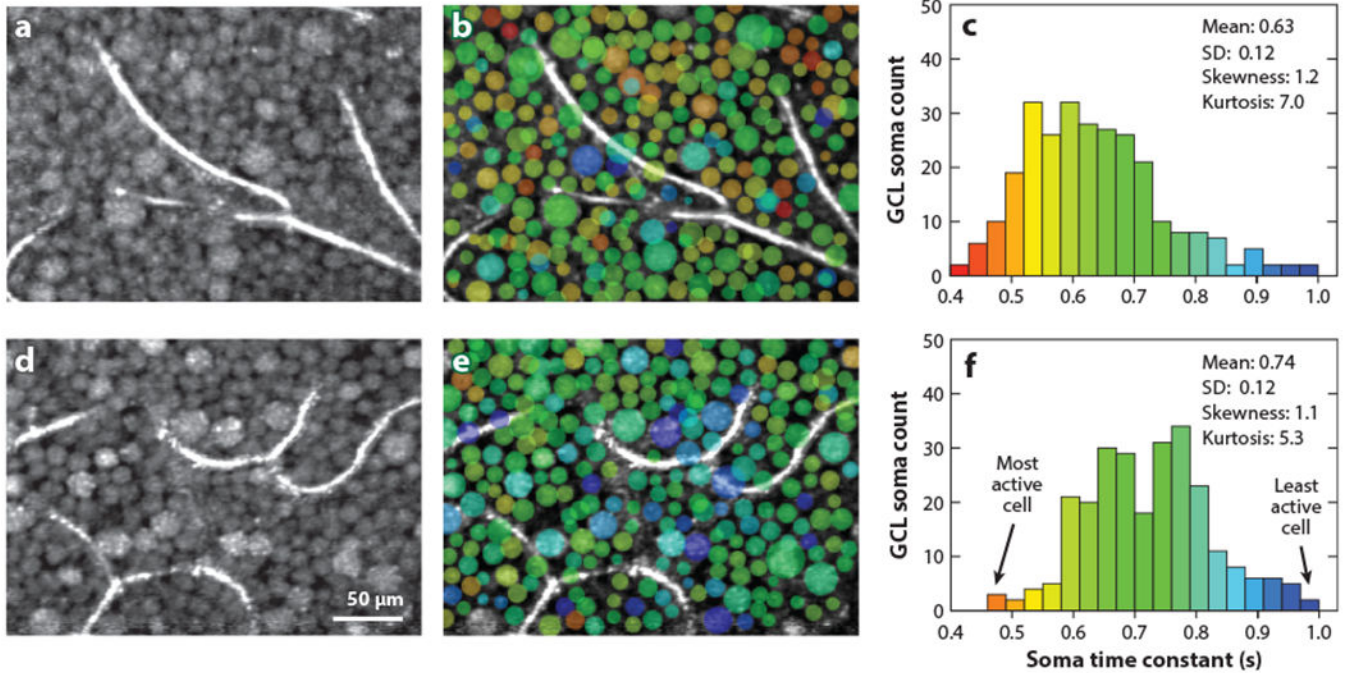
Figure 7.

The physiological response of a cone cell to light produces nanometer changes in its OS optical path length that we use to classify cones into spectral types. (*a*) Schematic shows the IS and OS of a cone cell and the underlying RPE cell that ensheathes it. The cone cell is stimulated with a visible flash during AO-OCT imaging, and a phase change results between the two bright reflections at opposing ends of the cone OS, which are labeled IS/OS and COST The plot shows the normalized sensitivity functions of the three cone types that are sensitive to short- (S), medium- (M), and long-wavelength (L) light (Stockman & Sharpe

2000). The vertical dashed line depicts the 637 nm peak of the example stimulus. (*b*) Phase response of cones is biphasic, with a rapid, shallow decrease in Δ*OPL* (*inset*) followed by a sustained increase whose amplitude varies with cone type (S, M, and L). The dashed gray line at 0 s represents the 5 ms stimulus flash. Individual traces of 1,094 cone cells are randomly colored. (*c*) En face intensity image shows the cone mosaic at 3.7° retinal eccentricity, as projected through its OSs. (*d*) The same cone mosaic is color-coded on the basis of cone classification (S in *blue*; M in green; L in *red*). Figure adapted from F. Zhang et al. (2019). Abbreviations: Δ*OPL*, change in optical path length; AO-OCT, adaptive optics optical coherence tomography; COST, cone outer segment tip; IS, inner segment; IS/OS, inner segment/outer segment junction; OS, outer segment; RPE, retinal pigment epithelium.
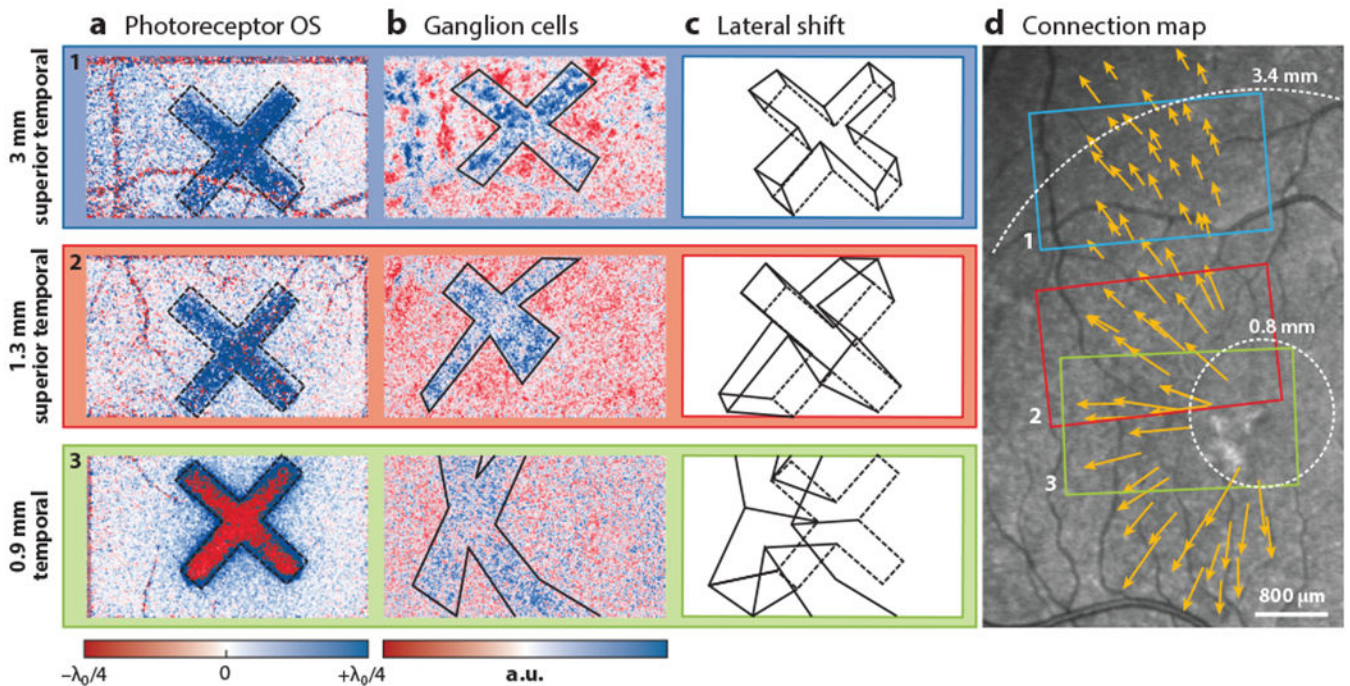
Figure 8.

Motion-evoked speckle changes with depth in the RPE–BM complex. (*a*) Averaged AO-OCT B-scan of a normal subject shows distinct hyper- and hyporeflective bands in the outer retina. Four depths are marked on the superimposed averaged A-line profile that represent the apical, middle, and basal sublayers of the RPE and the BM layer. (*b*) The color-coded correlation functions at the four corresponding depths, with fits to an exponential: $A\,\mathrm{e}^{-t/\tau} + B$, where τ is the time constant and A and B are fitting parameters. (*c*) The average time constants of four subjects. Error bars denote standard deviation. Figure adapted with permission from Liu et al. (2019b). Abbreviations: AO-OCT, adapted optics optical coherence tomography; BM, Bruch's membrane; COST, cone outer segment tip; ELM, external limiting membrane; IS/OS, inner segment/outer segment junction; ROST, rod outer segment tip; RPE, retinal pigment epithelium.

Figure 9.

Temporal dynamics vary between GCL somas in two normal subjects (*rows*). (*a,d*)
Registered and averaged amplitude-reflectance images of the GCL reveal a contiguous
mosaic of GCL somas disrupted only by capillaries. (*b,e*) Correlation time constants were
computed for individual somas and superimposed as semitransparent false colors, as defined
in the histograms in panels *c* and *f*. Note that some time constant values in panels *b* and *e* are
superimposed on capillaries and on each other, as soma centers at these locations lie at
different depths than those of the images. Figure adapted from Kurokawa et al. (2020).
Abbreviations: GCL, ganglion cell layer; SD, standard deviation.

Figure 10.
Simultaneous optical path length changes within the cone OS and between the GCL and IPL of the inner retina in response to an X-shaped, white light stimulus. As indicated by the correspondingly colored rectangles in the fundus image at right, retinal locations are at (*top row*) 3 mm superior temporal, (*middle row*) 1.3 mm superior temporal, and (*bottom row*) 0.9 mm temporal from the fovea. Phase response was observed (*a*) in the cone OS and (*b*) between the GCL and IPL layers. The borders of the responding retinal regions were traced manually. In the left colored response bar, λ_o is the center wavelength of the imaging light source, 841.5 nm, which gives an optical path length range of approximately −210 nm to +210 nm. The right colored response bar is specified in arbitrary units (a.u.), as the much smaller response was known with less certainty. (*c*) The lateral shift between the cone and GCL–IPL responding areas is visualized by superimposing their traced areas in panels *a* and *b*. (*d*) SLO image (Spectralis, Heidelberg Engineering) of the subject is superimposed with orange vectors denoting displacements of GCL–IPL excitation from cone OS excitation. White circles are concentric to the macular center. Figure adapted with permission from Pfäffle et al. (2019). Abbreviations: GCL, ganglion cell layer; IPL, inner plexiform layer; OS, outer segment; SLO, scanning laser ophthalmoscopy.

Table 1

Interpretation of cone photoreceptor reflections in Supplemental Video 1

Frame number(s)	Depth location	Description
34–41	ONL, middle	Photoreceptor axons at interface between Henle's fiber layer and ONL somas
52–53	ONL, basal	Likely cone somas due to proximity to ELM
55–57	ELM	Mottled irregular reflection
58–61	Cone IS, apical	Diffuse reflection not confined to cones; suggestive of nonwaveguiding
62–67	Cone IS, basal	Punctated reflection internal to cones; suggestive of waveguiding
68–73	Cone IS/OS	Bright multimode reflection internal to cones (Jonnal et al. 2014, Liu et al. 2015); waveguided (Gao et al. 2008)
74–75	Cone IS/OS (S cones)	Sparse, bright reflections of S cones (see description in Section 4.1.1)
74–78	Cone OS	Dim reflections internal to cone segments; presumably waveguided; reflections internal to rod segments also appear to be present
81–86	COST	Bright single-mode reflections internal to cones (Liu et al. 2015, Jonnal et al. 2017); waveguided (Gao et al. 2008)

Abbreviations: COST, cone outer segment tip; ELM, external limiting membrane; IS, inner segment; IS/OS, inner segment/outer segment junction; ONL, outer nuclear layer; OS, outer segment.